# On the use of graph centralities to compute generalized inverse of singular finite element operators: applications to the analysis of floating substructures

Christophe Bovet

*Article Type*

# On the use of graph centralities to compute generalized inverse of singular finite element operators: applications to the analysis of floating substructures

Christophe Bovet*[1]

[1] *Onera – The French Aerospace Lab, F-92322 Châtillon, France*

**Correspondence:** Christophe Bovet. Email: christophe.bovet@onera.fr

Received March 11, 2022; Revised March 11, 2022; Accepted March 11, 2022

**Summary**

This article introduces a robust and affordable method to compute nullspace and generalized inverse of finite element operators involved in dual domain decomposition methods. The methodology relies on the operator partial factorization and on the analysis of a well chosen Schur complement. The sparse linear operator is interpreted as a network and graph centrality measures are used to select the condensation variables. Eigen vector, Katz and Page Rank centralities are evaluated. An extension to deal with symmetric indefinite systems arising from mixed finite elements is also presented. The approach is assessed on highly heterogeneous problems and one industrial application is presented: the numerical homogenization of solid propellant.

**Keywords:** Nullspace detection, generalized inverse, FETI, floating subdomain, fixing-node, graph centralities

## 1 Introduction

Domain decomposition methods such as the Finite Element Tearing and Interconnecting (FETI) [16] and its variants TFETI [13,28], HTFETI [34,38], AMPFETI [3–5], involve the resolution of semidefinite systems of equations. These systems arise when the automatic decomposition leads to subdomains whose are not subjected to sufficient Dirichlet boundary conditions to prevent the existence of rigid body motions. These subdomains are commonly denoted as "floating subdomains" (or substructures) [15]. The presence of floating substructures also occurs when studying free-free flexibility matrices for structural analysis [17].

FETI like methods are able to tackle really really large-size problems while exhibiting a good scalability [34, 43]. The the range of applications of these methods also grows notably covering for example, biomechanics [6], structural dynamics [30], contact mechanics [14], digital image correlation [2] and isogeometric analysis [20, 27].

Also, a continuous effort has been made to be able to deal with real engineering applications. These applications often exhibit pathological components that hinder the convergence of the underlying Krylov solver, such as jagged interfaces, bad aspect ratios, strong heterogeneities, incompressibility, etc. [25, 26]. These pathological components lead to highly ill-conditioned linear systems, making essential the use of enhanced iterative solvers. Two kinds of strategies have been proposed to increase the robustness of domain decomposition solvers. The first strategy relies on augmenting the Krylov solver with well chosen supplementary coarse space coming from the solution of local generalized eigenvalue problems for example [32, 39, 41]. The second one is to use a block Krylov solver [19] or a multipreconditioned Krylov solver [4, 8, 19, 35, 40].

If the improvement of the iterative interface solver is often pointed out, it is not the only component of the method put on severe test when dealing with ill-conditioned problems. The treatment of floating substructures through the automatic detection of local operator nullspaces and the computation of generalized inverses, are crucial points of the FETI methods. A misdetection of these kernels leads inevitably to the divergence of the iterative solver and ill conditioned generalized inverses may slow down its convergence. Since the seminal work of Farhat & Géradin [15], few authors have investigated the problem. A treatment of substructures with internal mechanisms was proposed in [37]. More recently, generalized inverse computation and regularization techniques have been proposed in the case of known nullspace [12]. The use of incomplete factorization, the concept of fixing-nodes and a selection process based on the Perron vector have been introduced [11]. The impact of the generalized inverse computation on the convergence of the iterative solver has been investigated in [29]. However, these research articles do not address the case of ill conditioned local operators and most of the examples remain academic. From our experience in the development of AMPFETI and from the simulation of ill-conditioned industrial applications, such as the numerical homogenization of woven composite [4] and solid propellant [5], a robust process to detect local operators nullspaces and to compute generalized inverse turns out to be essential. The aim of this paper is to present an extension of the approach proposed in [11] in order to deal with ill conditioned operators. We typically tackle the problem of material heterogeneity and highly variable finite element mesh size. A procedure for symmetric indefinite systems is also presented. To this end, we propose several strategies to improve the selection of fixing-nodes. Most of them are based on the notion of graph centrality. Also, we provide a simple process to handle symmetric indefinite system arising from mixed finite element method for instance.

The article is organized as follows: Section 2 recalls basic notions about generalized inverse and graph theory, Section 3 provides a short review on existing methods, while the overall methodology is introduced in Section 4.

Section 5 details all the fixing-nodes selection strategies. Three numerical examples are provided in Section 6, an academic Laplace problem, an academic elastic truncated pyramid and a an elastic simplified laminated composite. The first example is illustrative in order to understand how behave the centrality measures. The second example is a reproduction of the solid benchmark proposed in [11], it assesses the good performance of proposed methods. The latter example is a large ill-conditioned problem, it highlights the performance of the proposed approach and provides a comparison with the MUMPS automatic defect detection. The approach is assessed on the highly ill-conditioned problem of the numerical homogenization of solid propellant in Section 7. This application also shows the performance of the specific treatment of symmetric indefinite systems proposed in Section 5.3. Finally, Section 8 concludes the paper and draws some perspectives.

# 2 Notations and preliminaries

## 2.1 Generalized inverse

Let $\boldsymbol{\mathcal{A}} \in \mathbb{R}^{n\times n}$ be a real square, possibly singular, matrix, the $(i,j)$ component of the matrix $\boldsymbol{\mathcal{A}}$ is denoted $\mathcal{A}_{ij}$. In the following, $\boldsymbol{I}_n \in \mathbb{R}^{n\times n}$ is the identity matrix and $\boldsymbol{0}_n \in \mathbb{R}^{n\times n}$ the zero matrix. If $\alpha \subseteq \{1,\dots,n\}$ and $\beta \subseteq \{1,\dots,n\}$ are two nonempty subsets of $\{1,\dots,n\}$, we denote by $\boldsymbol{\mathcal{A}}_{\alpha\beta}$ the submatrix of $\boldsymbol{\mathcal{A}}$ with the components $(\mathcal{A}_{ij})_{i\in\alpha, j\in\beta}$. For convenience, if $\alpha \subseteq \{1,\dots,n\}$ is a nonempty subset, we denote by $\overline{\alpha}$ its complement $\overline{\alpha} = \{1,\dots,n\} \setminus \alpha$. For any nonempty $\alpha$ and after some permutations of rows and columns, the matrix $\boldsymbol{\mathcal{A}}$ can be written by block as :

$$\boldsymbol{\mathcal{A}}^\star = \boldsymbol{P}^\top \boldsymbol{\mathcal{A}} \boldsymbol{P} = \begin{bmatrix} \boldsymbol{\mathcal{A}}_{\alpha\alpha} & \boldsymbol{\mathcal{A}}_{\alpha\overline{\alpha}} \\ \boldsymbol{\mathcal{A}}_{\overline{\alpha}\alpha} & \boldsymbol{\mathcal{A}}_{\overline{\alpha}\overline{\alpha}} \end{bmatrix} \tag{1}$$

where $\boldsymbol{P}$ is a permutation matrix. In the following, we directly consider the form (1) and we omit the permutation matrices and the star exponent.

We are interested in finding a solution of the consistent linear system $\boldsymbol{\mathcal{A}}x = b$ where $\boldsymbol{\mathcal{A}} \in \mathbb{R}^{n\times n}$ is singular. The defect of the matrix $\boldsymbol{\mathcal{A}}$ is denoted $k$ and its rank $r = n - k$. This system of equation is consistent if $b \in \mathrm{Im}(\boldsymbol{\mathcal{A}})$. A well known method is to use the Moore-Penrose generalized inverse $\boldsymbol{\mathcal{A}}^\dagger$ which is the unique matrix satisfying the

four Moore-Penrose conditions (see Section 5.5.2 [18]).

$$\boldsymbol{\mathcal{A}}\boldsymbol{X}\boldsymbol{\mathcal{A}} = \boldsymbol{\mathcal{A}} \tag{2}$$

$$\boldsymbol{X}\boldsymbol{\mathcal{A}}\boldsymbol{X} = \boldsymbol{X} \tag{3}$$

$$\boldsymbol{\mathcal{A}}\boldsymbol{X} = (\boldsymbol{\mathcal{A}}\boldsymbol{X})^\top \tag{4}$$

$$\boldsymbol{X}\boldsymbol{\mathcal{A}} = (\boldsymbol{X}\boldsymbol{\mathcal{A}})^\top \tag{5}$$

The Moore-Penrose generalized inverse is computed through a singular value decomposition (SVD), $\boldsymbol{\mathcal{A}} = \boldsymbol{U}\boldsymbol{\Sigma}\boldsymbol{V}^\top$ where $\boldsymbol{U} \in \mathbb{R}^{n\times n}$ and $\boldsymbol{V} \in \mathbb{R}^{n\times n}$ are orthogonal matrices, the diagonal matrix $\boldsymbol{\Sigma} \in \mathbb{R}^{n\times n}$ contains all the singular value of $\boldsymbol{\mathcal{A}}$.

$$\boldsymbol{\Sigma} = \text{diag}(\sigma_1, \dots, \sigma_n) \quad \text{with} \quad \sigma_1 \geq \sigma_2 \cdots \geq \sigma_r > \sigma_{r+1} = \cdots = \sigma_n = 0$$

The Moore-Penrose generalized inverse is given by $\boldsymbol{\mathcal{A}}^\dagger = \boldsymbol{V}\boldsymbol{\Sigma}^\dagger\boldsymbol{U}^\top$ where $\boldsymbol{\Sigma}^\dagger = \text{diag}(\sigma_1^{-1}, \dots, \sigma_r^{-1}, 0, \dots, 0)$. The Moore-Penrose generalized inverse is often considered as the "best generalized inverse" since it minimizes the Frobenius norm $\|\boldsymbol{\mathcal{A}}\boldsymbol{X} - \boldsymbol{I}_n\|_F$. It is however very expensive to evaluate, common algorithms have complexities in $O(n^3)$. Considering the treatment of floating subdomains in dual domain decomposition methods, any matrix satisfying (2) is suitable and it is not necessary to fulfill all Moore-Penrose conditions. This work proposes a robust but cheap methodology to compute such a matrix.

## 2.2 Recall on graphs

The present work makes use of tools coming from Graph (also called network) theory, useful notions are recalled hereafter. Reader interested in a wider documentation can refer to [36].

**Undirected graph** A graph $\mathcal{G}$ is defined by two sets $(V, E)$. The first set $V$ is a collection of vertices while the second set $E$ contains edges. An edge is a pair of vertices $(u, v) \in V \times V$ that represents some kind of link between $u$ and $v$. If this link does not depend on the ordering, the graph is said undirected. In this work, we only consider undirected simple graphs e.g. graphs without any self-edge[1] nor multi-edge. From now on, we denote by $n_v$ the number of vertices and by $n_e$ the number of edges.

**Weighted graph** It will be useful to characterize the strength of an edge. The strength of the link between $u$ and $v$ can be characterized by a strictly positive scalar $\omega_{uv} > 0$ $(u, v) \in E$. A weighted graph is thus defined by a graph and a set of weight $\mathcal{G}_{\omega_e} = (\mathcal{G}, \omega_e)$ with $\omega_e \in (\mathbb{R}^{+*})^{n_e}$.

[1] A self-edge is a pair $(u, u), u \in V$

**The adjacency matrix** The adjacency matrix of the graph is the matrix $\boldsymbol{A} \in \mathbb{R}^{n_v \times n_v}$ with elements $a_{uv}$ such that

$$a_{uv} = \begin{cases} \omega_{uv} > 0 \text{ if there is an edge between vertices } u \text{ and } v \\ 0 \qquad\quad \text{otherwise.} \end{cases}$$

In the case of unweighted graphs, $a_{uv} = 1$ if the vertices $u$ and $v$ are linked. In this work, we only consider undirected simple graphs so $\boldsymbol{A}$ remains symmetric and since self-edges are not taken into account in this work we have $a_{uu} = 0 \; \forall u$.

**Degree of a vertex** The degree of a vertex $u$ is the scalar $d_u = \sum_{v=0}^{n_v} a_{uv}$. Let $\boldsymbol{D}$ be the diagonal matrix of order $n_v$ such that $\boldsymbol{D} = \text{diag}(d_1, \ldots, d_{n_v})$. For undirected unweighted graph, the degree $d_u$ is simply the number of edges connected to $u$.

**The graph Laplacian** The graph Laplacian is alternative representation of undirected weighted graph. The matrix form of the graph Laplacian is the matrix $\boldsymbol{L} \in \mathbb{R}^{n_v \times n_v}$ defined by $\boldsymbol{L} = \boldsymbol{D} - \boldsymbol{A}$. The matrix $\boldsymbol{L}$ remains symmetric. The graph Laplacian, has various applications such as graph partitioning or network visualization (see for example Section 6.14 in [36]).

**Graph centrality** One of the frequent applications of graph theory tools is to find out which vertex is the most important in a network. This importance can be described in several ways, which translate into different measures of graph centrality. These measures usually depends on the graph topology and on the strength of the graph edges. It will be defined by a score vector $\boldsymbol{c} \in \mathbb{R}_+^{n_v}$. The graph centralities used in this work will be presentend in Section 5.2.

# 3 Brief review of existing approaches

## 3.1 The pioneering work of Farhat and Géradin

Farhat & Géradin [15] were the first to investigate the treatment of floating subdomains in structural mechanics. They proposed three strategies to cheaply compute the generalized inverse and the nullspace of the stiffness matrices.

The first one relies on the null pivots detection of the Crout factorization with symmetric pivoting. Indeed, if the $k$ null pivots are put in the set $\overline{\alpha}$, both

$$\begin{bmatrix} \boldsymbol{\mathcal{A}}_{\alpha\alpha}^{-1} & \boldsymbol{0} \\ \boldsymbol{0} & \boldsymbol{0} \end{bmatrix} \quad \text{and} \quad \begin{bmatrix} \boldsymbol{\mathcal{A}}_{\alpha\alpha}^{-1} & -\boldsymbol{\mathcal{A}}_{\alpha\alpha}^{-1}\boldsymbol{\mathcal{A}}_{\alpha\overline{\alpha}} \\ \boldsymbol{0} & \boldsymbol{I}_k \end{bmatrix} \tag{6}$$

fulfill the first Moore-Penrose condition (2) and a basis of the nullspace is given by the $n \times k$ matrix $\boldsymbol{R}$.

$$\boldsymbol{R} = \begin{bmatrix} -\boldsymbol{\mathcal{A}}_{\alpha\alpha}^{-1}\boldsymbol{\mathcal{A}}_{\alpha\overline{\alpha}} \\ \boldsymbol{I}_k \end{bmatrix} \tag{7}$$

The defect computation relies on the distinction between null and small pivots which requires an user defined small constant $\varepsilon$. This parameter may be hard to setup in presence of ill conditioned systems. A "modern" version of this approach is to let up-to-date direct solvers, such as MUMPS [1] or Dissection [42], detect null pivots and compute the generalized inverse and nullspace. As will be shown in Section 6.3, even the most advanced solvers such as MUMPS can be put in severe test with specific pathological tests.

The second method proposed in [15] needs to know *a priori* an upper bound of the defect $q$. A Crout factorization without pivoting is performed up to the step $n - q + 1$, then a SVD is applied on the remaining Schur complement to obtain the true defect $k$. The rest of the factorization is done with full pivoting and last $k$ pivots are considered as null pivots. This method still relies on an user defined constant but the SVD is applied on a small Schur complement with a better condition number.

The third method, initially thought for structural mechanics, needs to know the nullspace in the case of a totally unrestrained subdomain i.e. a subdomain without any Dirichlet boundary condition. Let $\boldsymbol{R}_u$ be a basis of this totally unrestrained nullspace. In the context of 3D elastostatics, if the subdomain is connexe, without mechanism and totally unrestrained, this nullspace known. It is composed of the six rigid body modes (3 translations and 3 rotations). These rigid body modes can be built explicitly using a geometric procedure. For an unrestrained subdomain, the generalized inverse can be computed using (6) and considering the six last pivots as null pivots. For partially restrained subdomains the strategy is slightly more complex. Let $n_D$ be the number of unknowns subjected to Dirichlet boundary conditions. A boolean matrix $\boldsymbol{E}$ of size $n \times n_D$ is introduced with $e_{ij} = 1$ if the unknown $j$ is constrained by the i-th boundary condition and $e_{ij} = 0$ elsewhere. A SVD is then performed on the matrix $\boldsymbol{Z} = \boldsymbol{E}^\top \boldsymbol{R}_u$ to compute the actual defect of the operator $\boldsymbol{\mathcal{A}}$. The actual nullspace which is a linear combination of the columns of $\boldsymbol{R}_u$ can also be retrieved from the singular value decomposition. Once the defect $k$ is known, the generalized inverse can also be computed considering the last $k$ pivots as null pivots. From a mechanical point of view, the matrix $\boldsymbol{Z}$ looks like the virtual work produced by the Dirichlet boundary conditions when considering rigid body motions as virtual displacements. Again, the defect computation involves a small constant for the SVD of the matrix $\boldsymbol{Z}$. Since both $\boldsymbol{E}$ and $\boldsymbol{R}_u$ are purely "kinematic", the defect is insensitive to the condition number of the stiffness matrix. This property may be useful when dealing with highly heterogeneous subdomains. Only the condition number of the generalized inverse will be impacted. The condition number of $\boldsymbol{R}_u$ depends however on the

slenderness of the subdomain. Scaling procedures have been proposed in [37] to improve this point. This algebraic–geometric method requires the absence of internal mechanism. Their detection and removal have been investigated in [15] with the mechanism buster algorithm and this constraint has been overcome few years later with geometric procedures [37]. This method is however hard to generalize to meshes composed of exotic element types such as, cohesive zone elements [31] or pressure-displacement mixed elements [45] or multipoint constraints (MPC).

### 3.2 The incomplete factorization and fixing-nodes framework

The previous methods are focused on the defect computation, they do not investigate the condition number of the resulting generalized inverse. A continuous progress has been made in this field by the research group of Z. Dostál [11, 12, 22, 23, 29] which led to the incomplete factorization framework and the concept of fixing-nodes.

As pointed out in [11], all previous methods can be reformulated in the incomplete factorization framework. Only symmetric semi-definite matrices are considered in [11] and the framework is expressed in terms of incomplete Cholesky factorization. If the symmetry provides useful properties such as the Haynsworth inertia additivity formula, it is not a limitation of the approach. In the following, we use the incomplete $\boldsymbol{LU}$ factorization. In the case of a symmetric semi-definite matrix, one simply has to replace all matrices $\boldsymbol{U}$ by $\boldsymbol{L}^\top$.

If $c$ is a non empty subset of $\{1, \dots n\}$, the incomplete $\boldsymbol{LU}$ factorization is

$$\boldsymbol{\mathcal{A}} = \begin{bmatrix} \boldsymbol{\mathcal{A}}_{\overline{cc}} & \boldsymbol{\mathcal{A}}_{\overline{c}c} \\ \boldsymbol{\mathcal{A}}_{c\overline{c}} & \boldsymbol{\mathcal{A}}_{cc} \end{bmatrix} = \begin{bmatrix} \boldsymbol{L}_{\overline{cc}} & \boldsymbol{0} \\ \boldsymbol{L}_{c\overline{c}} & \boldsymbol{I} \end{bmatrix} \begin{bmatrix} \boldsymbol{U}_{\overline{cc}} & \boldsymbol{U}_{\overline{c}c} \\ \boldsymbol{0} & \boldsymbol{S}_{cc} \end{bmatrix}. \tag{8}$$

As long as $\boldsymbol{\mathcal{A}}_{\overline{cc}}$ remains full rank, a generalized inverse of $\boldsymbol{\mathcal{A}}$ is given by

$$\boldsymbol{\mathcal{A}}^+ = \begin{bmatrix} \boldsymbol{U}_{\overline{cc}}^{-1} & -\boldsymbol{U}_{\overline{cc}}^{-1}\boldsymbol{U}_{\overline{c}c}\boldsymbol{S}_{cc}^\dagger \\ \boldsymbol{0} & \boldsymbol{S}_{cc}^\dagger \end{bmatrix} \begin{bmatrix} \boldsymbol{L}_{\overline{cc}}^{-1} & \boldsymbol{0} \\ -\boldsymbol{L}_{c\overline{c}}\boldsymbol{L}_{\overline{cc}}^{-1} & \boldsymbol{I} \end{bmatrix}. \tag{9}$$

Since the Schur complement $\boldsymbol{S}_{cc}$ is a small dense matrix, the use of the Moore-Penrose generalized inverse is reliable and affordable here. The matrix $\boldsymbol{\mathcal{A}}_{\overline{cc}}$ being full rank, the Schur complement is rank deficient due to the property

$$det(\boldsymbol{\mathcal{A}}) = det(\boldsymbol{S}_{cc}) \cdot det(\boldsymbol{\mathcal{A}}_{\overline{cc}})$$

For well conditioned test cases, the use of a "large enough" set $c$, for which $\text{card}(c) > k$, suffices. For ill conditioned systems however, to choose good *candidates* for the incomplete factorization remains essential, in order to get $\boldsymbol{\mathcal{A}}_{\overline{cc}}$ and $\boldsymbol{\mathcal{A}}^+$ reasonably well conditioned, and to facilitate determination of the defect of $\boldsymbol{S}_{cc}$. In [11], nodes of the mesh

corresponding to the unknowns of the set $c$ are called fixing-nodes. Since these fixing-nodes define the unknowns used for the static condensation. The attributes "fixing" and "condensation" are used interchangeably in the following. Also, for symmetric indefinite systems, we will use the term fixing-variables since all variables of fixing-nodes will not be put in the set $c$.

From a mechanical point of view, these fixing-nodes must not be aligned, and well distributed within the substructure. From these considerations, a two-step construction process has been proposed in [11]. First, the subdomain mesh is virtually split into $M \geq k$ parts (also called color in the following). Then a fixing-node close to the center of each color is selected using an heuristic.

# 4 Overall methodology

This section introduces the overall methodology to detect the nullspace and to compute the generalized inverse. It follows the two-steps construction process proposed in [11]. As before, the subdomain mesh is virtually split into $M \geq k$ parts, then one fixing-node is selected in each part. Please note that, if the initial subdomain is not connexe, the number of part must be adapted. Since an upper bound of the defect is usually known for a connexe subdomain, the overall methodology is logically applied to each connected components of the subdomain.

However, the selection strategy of fixing-node is improved in order to tackle highly ill-conditioned systems. Indeed, to pick-up a fixing-node close to the center of each color is not sufficient for ill-conditioned system such as highly heterogeneous problems. The fixing-variables $c$ should correspond to large diagonal terms in the matrix in order to improve the condition number of $\boldsymbol{\mathcal{A}}_{\overline{cc}}$ and $\boldsymbol{\mathcal{A}}^{+}$ and to facilitate the estimation of the defect of the matrix. The methodology is summed up in Algorithm 1 and illustrated with Figure 1.

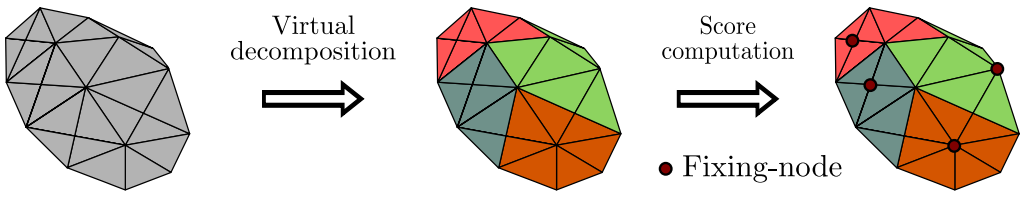


Figure 1: Schematic representation of the overall methodology.

## 4.1 Selection process of fixing-nodes

In this work, several selection strategies are proposed and compared, they will be detailed in Section 5. We only give the common framework here. These selection strategies can be expressed as a vector-valued function $f$ of some

**Algorithm 1** Fixing-nodes selection algorithm

Verify that the initial mesh in connexe (if not apply Algorithm 1 to each connected component).
Virtually split the mesh in $M$ connexe parts
**for** each part **do**
    Apply selection strategy (see Section 5)
**end for**
Filter duplicates nodes if needed
Filter mixed variables if needed (see Section 5.3)

graph $\mathcal{G}$ such as $f(\mathcal{G}) = \boldsymbol{s} \in \mathbb{R}^{+p}$ where $p$ is the number of nodes of the considered color. All components of the vector $\boldsymbol{s}$ are positive, they traduce the score of the corresponding node. The node with the highest score is selected as the fixing-node. The application of this selection process to each color provides a set of fixing-nodes, all unknowns linked to these nodes are put in the set of fixing-variables $c$. Once the set of fixing variables is defined, the incomplete factorization is performed (8).

## 4.2 Nullspace computation and generalized inverse of the Schur complement

The incomplete factorization framework leads to a small dense Schur complement $\boldsymbol{S}_{cc}$ of order $m$. The matrix $\boldsymbol{\mathcal{A}}_{\overline{cc}}$ being full rank, the Schur complement is rank deficient. The use of the Moore-Penrose generalized inverse is affordable and applied here. The singular value decomposition, $\boldsymbol{S}_{cc} = \boldsymbol{U}\boldsymbol{\Sigma}\boldsymbol{V}^\top$ where $\boldsymbol{U}$ and $\boldsymbol{V}$ are orthogonal matrices. The diagonal matrix $\boldsymbol{\Sigma}$ contains all the singular values of $\boldsymbol{S}_{cc}$.

$$\boldsymbol{\Sigma} = \mathrm{diag}(\sigma_1, \ldots, \sigma_m) \quad \text{with} \quad \sigma_1 \geq \sigma_2 \cdots \geq \sigma_r > \sigma_{r+1} = \cdots = \sigma_m = 0$$

The Moore-Penrose generalized inverse is given by $\boldsymbol{S}_{cc}^\dagger = \boldsymbol{V}\boldsymbol{\Sigma}^\dagger\boldsymbol{U}^\top$ where $\boldsymbol{\Sigma}^\dagger = \mathrm{diag}(\sigma_1^{-1}, \ldots, \sigma_r^{-1}, 0, \ldots, 0)$. The nullspace of the Schur complement $\boldsymbol{R}_c$ is the $(m-r)$ last columns of the matrix $\boldsymbol{V}$. The nullspace of the full matrix is deduced from $\boldsymbol{R}_c$

$$\boldsymbol{R} = \begin{bmatrix} -\boldsymbol{\mathcal{A}}_{\overline{cc}}^{-1}\boldsymbol{\mathcal{A}}_{\overline{c}c}\boldsymbol{R}_c \\ \boldsymbol{R}_c \end{bmatrix} \tag{10}$$

The estimation of the rank of $\boldsymbol{S}_{cc}$ involves a user defined threshold $\epsilon$ to distinguish between null singular values and small ones. Two criterion are classically used. The first one compare the current singular values with respect to the largest one

$$\text{Relative criterion:} \quad \sigma_j \leq \epsilon\, \sigma_1 \tag{11}$$

Another possibility is to look for the jump between two adjacent singular values

$$\text{Jump criterion:} \quad \sigma_{j+1} \leq \epsilon \sigma_j \tag{12}$$

If the selection strategy is well chosen, both criteria behave similarly most of the time and the validity range of the threshold covers several decades. The jump criterion may have the advantage when several jump of material coefficients are present in the underlying physical problem.

More complex strategy may be proposed, based on unsupervised learning for example. Indeed, the problem can be reformulated as a clustering problem where the singular values of the Schur complement are the sample data. The clustering problem intends to split singular values into two clusters corresponding to null and not null singular values. Several models of the machine learning scikit-learn library[2] have been tried in this work such as Gaussian mixture model and K-means. However, these advanced techniques have been used as is, without prior training. We were not able to build a clustering process outperforming the classical criteria especially for indeterminate cases such as symmetric indefinite systems (see Section 7.0.3). The sample data are probably too scarce. In the context of domain decomposition method, an interesting possibility is to share the singular values of all local stiffness operators to increase the number of data.

## 4.3 Some practical remarks

**About the number of fixing-nodes** An important parameter of the method is the number of condensation nodes. This number must be large enough to remove the non-trivial nullspace of the operator. For example, three nodes per connected component suffice for a 3D mechanical problem. For very heterogeneous problems and depending on the type of centrality used, it is possible that two colors select the same node. This node being at the interface between these two colors. This problem can be solved simply by slightly increasing the number of condensation nodes. For 3D mechanical problems, four condensation nodes per connected component are enough most of the time. Another strategy is to process the color successively. If a color proposes an already selected node, this node is refused and the second best node is picked up.

**About the implementation** The virtual split is performed using an automatic graph partitioner such as METIS or Scotch. The condensation node selection method is easily implemented in parallel. Each color is processed independently with shared memory parallelism. For graph centralities that require solving linear systems, iterative solvers with low memory cost are used.

[2] See https://scikit-learn.org/

# 5 On the choice of fixing-nodes

In this section, we present different strategies for choosing fixing-nodes. Most of them take advantage of graph theory and in particular of the notion of centrality. Proposed strategies have to bear in mind various objectives:

- to lead to good fixing-nodes candidates, which means to minimize the condition number of operators, and to give a clear distinction between null and small singular values.
- to present small computational cost
- to be robust (meaning that the determination barely fail)

## 5.1 Taking into account the operator

Different graphs naturally arise in the context of finite element problems. The finite element mesh, via its connectivity table, defines a first graph where the vertices are the nodes of the mesh and two nodes are linked by an edge if they belong to the same element. Also, the finite element operator can be considered as a graph where the vertices are the degrees of freedom. An edge links two degrees of freedom if there is an associated non-zero extra-diagonal term. In the present work, we choosed to use the "nodal" graph because of its smaller size. We note however that for very anisotropic problems, the latter option may be more suited.

### 5.1.1 Edge weights approximation

The finite element operator provides a natural way to define the strength of an edge. Indeed, the strength of the link between two vertices can be defined by the amplitude of the extra-diagonal term. This vision has been exploited successfully by algebraic multigrid methods [9], where depending on the value of the extra-diagonal term, one unknown strongly depends (or strongly influences) another.

The main difference here is that the vertices of the graph are the node of the mesh. So except for the case of the Poisson problem, there is not a direct mapping between nodes and degrees of freedom. Several edge weights may be proposed:

- **Full weight:** Let $\delta_u$ (resp. $\delta_v$) be the set of degrees of freedom associated with the node $u$ (resp. $v$). For two linked nodes $u$ and $v$, the full weight of the edge $(u, v)$ is defined as the sum of all extra diagonal terms

$$\omega_{uv} = \sum_{i \in \delta_u} \sum_{j \in \delta_v} |\mathcal{A}_{ij}|$$

.

- **Lumped weight:** Degrees of freedom are associated with physical quantities (temperature, displacement, etc.). Let $\phi^i$ be the physical quantity associated with the unknown $i$. The lumped weight of the edge is defined as the sum of all extra diagonal terms corresponding to the same physical quantity.

$$\omega_{uv} = \sum_{i \in \delta_u, j \in \delta_v, \phi^i = \phi^j} |\mathcal{A}_{ij}|$$

  .

- **Uniform weight** : all edges have a weight equal to 1.

The finite element operator is a sparse matrix that is stored most of the time in the CSC or CSR format. Looking up for a specific term in $\boldsymbol{\mathcal{A}}$ involves a binary search which is costly. Also, the lumped and full edge weight leads to the same centrality measure for isotropic problems. For this reason, the full weight version is not considered in the following.

## 5.2 Available selection methodologies

All the methods presented here can be put in the form of a vector function of the considered graph such as $f(\mathcal{G}) = \boldsymbol{s} \in \mathbb{R}^{+n_v}$. We assume that all components of the score vector $\boldsymbol{s}$ are positive. The node chosen as the fixing-node is the one with the highest score.

### 5.2.1 Random selection

Attributing randomly a score to each node is the simplest possible strategy. This approach has been proposed for the HTFETI method [33] where the choice of the fixing-nodes is based on a random number generator. For a homogeneous problem with a ruled mesh, it has been shown that the probability of a "bad choice" decreases strongly with the number of fixing-nodes. Here a "bad choice" corresponds to the choice of collinear nodes. It seems difficult to improve this approach to deal with ill conditioned cases, except from increasing the number of fixing-nodes.

### 5.2.2 Gravity center

Bearing in mind that the fixing-nodes must be evenly distributed over the subdomain, one possible approach is to select the closest node to the center of gravity of each subpart. Let $\boldsymbol{m}_i \in \mathbb{R}^3$ be the position vector of the node $i$. An approximation of this gravity center may be:

$$\boldsymbol{m}_g = \frac{\sum_{j=1}^{n} \varpi_j \boldsymbol{m}_j}{\sum_{j=1}^{n} \varpi_j} \tag{13}$$

where $\varpi_j$ is a weight associated with the node $j$. For node $i$, the score is defined as

$$s_i = \frac{1}{1 + \|\boldsymbol{m}_i - \boldsymbol{m}_g\|_2} \tag{14}$$

such that the closer node $i$ is to the center of gravity, the higher the score is. This geometric approach is simple but to choose appropriate weights is an inextricable task. Assigning an equal weight to all the nodes of the mesh will select one close to very refined area. For homogeneous problem, this is typically a bad choice since small elements are softer than larger ones (see Figure 2). A weight proportional to the diagonal terms of the stiffness matrix may

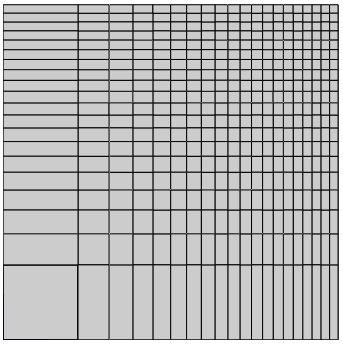

Figure 2: Small counter example: homogeneous material with variable mesh size.

seems a better choice but it is easy to find simple examples where this strategy fails (see for example Figure 3).

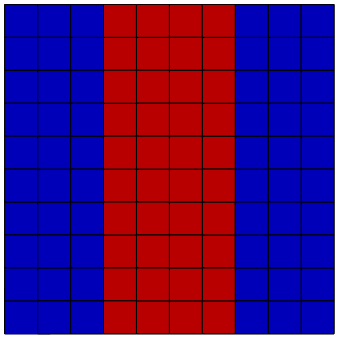

Figure 3: Small counter exemple: heterogeneous material where the red part is mush softer than the blue ones. Whatever the weight, a gravity center based method will always select the central node.

#### 5.2.3 Eigenvector centrality

Let $\{\lambda_i, \boldsymbol{q}_i\}_{1 \leq i \leq n_v}$ be the eigenmodes of the adjacency matrix $\boldsymbol{A}$ with $\lambda_1 \geq \lambda_2 \cdots \geq \lambda_{n_v}$. The eigenvector centrality is simply defined by the components of the dominant eigenvector $\boldsymbol{s} = \boldsymbol{q}_1$. All components of this dominant eigenvector,

also known as the Perron vector, are of the same sign thanks to the Perron–Frobenius theorem. We assume are that $\boldsymbol{q}_1$ is positive. With this centrality measure, the centrality of a node $i$ is proportional to the sum of the centralities of its neighbors. Thus a node can achieve a high centrality score either by having a lot of neighbors with average centrality, or by having a few neighbors with high centrality. Since $\boldsymbol{A}$ is symmetric, the evaluation of this centrality measure is really inexpensive and few steps of the Lanczos method leads to a good approximation. The use of the eigenvector centrality has already been proposed by [11], the adjacency matrix considered was associated with the unweigted graph. In this work, the eigenvector centrality is computed on the weighted graph which allows to take into account material heterogeneity for instance.

#### 5.2.4 Katz centrality

The Eigenvector centrality is only influenced by the edges of the graph. In our application, it turns out to be useful to add an intrinsic contribution to the centrality of each node. Since, from a mechanical point of view, nodes associated with stiff elements are obviously good fixing-node candidates. We would like to assign a specific importance to each node based on the diagonal terms of the stiffness matrix. The Katz centrality [24] (see also Section 7.1.3 in [36]) allows such a behavior, it is the solution of the system

$$(\boldsymbol{I} - \alpha^\star \boldsymbol{A})\boldsymbol{s} = \boldsymbol{\beta} \tag{15}$$

where $\alpha^\star$ is a scalar parameter and $\boldsymbol{\beta} \in \mathbb{R}^{n_v}$ is the intrinsic part of the centrality. The parameter $\alpha^\star$ has to be in the interval $[0, \lambda_1^{-1}[$, where $\lambda_1$ is the largest eigenvalue of $\boldsymbol{A}$. It is convenient to express this parameter with respect to $\lambda_1$ to get a robust process, the new parameter is $\alpha \in [0, 1[$, such that $\alpha^\star = \alpha\lambda_1^{-1}$.

The value of the intrinsic personality vector $\boldsymbol{\beta}$ is a parameter of the method. It has to be consistent with the choice made for the edges weights. Thus, all nodes have the same intrinsic centrality equal to 1 if the uniform edge weight is chosen. If full or lumped edge weight are used, the intrinsic personality of node $u$, $\beta_u$ is defined as:

$$\beta_u = \sum_{i \in \delta_u} |\mathcal{A}_{ii}|$$

where $\delta_u$ be the set of degrees of freedom associated with the node $u$.

From a computational point of view, the Katz centrality remains cheap since it only requires the estimation of the largest eigenvalue of $\boldsymbol{A}$ and the resolution of (15). The latter system which is symmetric positive definite, can be easily to solve with an iterative solver such as the Conjugate Gradient. The dominant eigenvector $\boldsymbol{q}_1$ is a good initial estimate.

#### 5.2.5 PageRank centrality

With the Katz centrality, a node shares its centrality whatever the number of its neighbors. It may be undesirable when the graph exhibits a large vertex degree variation. The PageRank centrality has been proposed to attenuate this phenomenon [10]. Here, the centrality shared by a node to its neighbors is divided by its degree. Then nodes that point to many others pass only a small amount of centrality on to each of those others, even if their own centrality is high. The PageRank centrality is the solution of the system

$$(\boldsymbol{I} - \alpha^\star \boldsymbol{A}\boldsymbol{D}^{-1})\boldsymbol{s} = \boldsymbol{\beta} \tag{16}$$

where, as in the Katz centrality, $\alpha^\star \in [0, 1[$, $\boldsymbol{\beta} \in \mathbb{R}^{n_v}$ is the intrinsic part of the centrality. The diagonal matrix $\boldsymbol{D}$ is the diagonal matrix degree. By construction, the graph is free of any isolated vertex so all diagonal terms are strictly positive. The intrinsic personality vector $\boldsymbol{\beta}$ is defined as in Section 5.2.4. In contrast with the Katz centrality, the computation of the largest eigenvalue of $\boldsymbol{A}$ is no more needed. The system (16) is however unsymmetric, it is solved with a stabilized BiCG.

#### 5.2.6 Cross-eigenvector

Most of the previous approaches make use of the adjacency matrix. An alternative method using the Laplacian matrix has been proposed in [21]. The score vector called Cross-eigenvector requires the computation of the eigenvectors associated with the smallest eigenvalues of the Laplacian matrix. A comparison with the Eigenvector centrality for an homogeneous Laplace problem has been provided in [21], showing the good performance of the Cross-eigenvector. However, for three dimensional problems, the four smallest eigenvalues of the Laplacian matrix are needed. Computing the smallest eigenvalues is a complex and costly task especially when the system is ill conditioned. This method has not be considered further in this work.

### 5.3 Treatment of symmetric indefinite systems

Symmetric indefinite systems occurs in many computational science and engineering. In the domain of computational mechanics, it naturally arises when studying problems involving mixed finite elements such as the Navier-Stokes equation in fluid mechanics or in the analysis of almost incompressible material with three fields mixed elements (see [7] and [45] Sections 2.6 and 5.5). For these problems, matrices are *highly indefinite* in the sense that they have many eigenvalues of both signs. Moreover, the unknowns are linked to various physical quantities: pressure, velocity in the former case and displacement, pressure, change of volume in the latter one. If neither specific row-column scaling nor nondimensionalization are performed, matrices are usually ill conditioned. Typically, the stiffness operator

obtained with three field mixed elements exhibits small negative eigenvalues. The presence of these small negative eigenvalues makes the computation of generalized inverse arduous. Indeed, without any specific treatment the Schur complement $\boldsymbol{S}_{cc}$ also possesses eigenvalues of both signs. The distinction between singular values associated with small negative eigenvalues due to the mixed form and small positive eigenvalues induced by the presence of rigid body motions becomes unclear.

Here, the addition theorem for Schur complements of Hermitian matrices (see [44] Chapter 1), also called Haynsworth inertia additivity formula, is an useful tool. The inertia of a Hermitian matrix $\boldsymbol{\mathcal{A}}$ (symmetric in our case) is defined as the ordered triplet

$$\mathrm{In}(\boldsymbol{\mathcal{A}}) = (p(\boldsymbol{\mathcal{A}}), q(\boldsymbol{\mathcal{A}}), n(\boldsymbol{\mathcal{A}}))$$

whose components are respectively the numbers of positive, negative, and zero eigenvalues of $\boldsymbol{\mathcal{A}}$. Still considering a splitting of the form (8) and assuming $\boldsymbol{\mathcal{A}}_{\overline{cc}}$ nonsingular, the addition theorem for Schur complements of Hermitian matrices states that

$$\mathrm{In}(\boldsymbol{\mathcal{A}}) = \mathrm{In}(\boldsymbol{\mathcal{A}}_{\overline{cc}}) + \mathrm{In}(\boldsymbol{S}_{cc}).$$

Thus, to avoid $\boldsymbol{S}_{cc}$ having negative eigenvalues, it suffices to force them to be in the spectrum of $(\boldsymbol{\mathcal{A}}_{\overline{cc}})$. In the context of mixed finite element, after the selection of fixing-nodes, a simple way to proceed is to remove all unknowns associated with mixed variables from the set $c$. The benefit of this approach is exemplified in Section 7.

# 6 Numerical examples

In [11], the quality of a generalized inverse is evaluated from the violation of the Moore-Penrose conditions (2)-(5), and regarding the effective condition number of $\boldsymbol{\mathcal{A}}^{+}$ and the condition number of $\boldsymbol{\mathcal{A}}_{\overline{cc}}$. The effective condition number is defined as

$$\overline{\mathrm{cond}}(\boldsymbol{\mathcal{A}}) = \frac{\lambda_1}{\lambda_r}$$

where $\lambda_1$ is the largest eigenvalue and $\lambda_r$ is the smallest not null eigenvalue. The classical condition number of an invertible matrix $\boldsymbol{M}$ is denoted $\mathrm{cond}(\boldsymbol{M})$. In this study, we limit our attention to the these two condition numbers. Again, to compute the small eigenvalues of ill-conditioned matrices is a complex task. These condition numbers are only computed for the academic examples in Section 6.1 and Section 6.2. For large scale examples, the performance of the method is analyzed with respect to the validity range of the threshold involved in the defect computation of the Schur complement $\boldsymbol{S}_{cc}$.

**Remarks on the implementation and hardware computing resources** All strategies have been implemented in the AMPFETI module of the finite element suite Z-set [3]. The MUMPS[4] solver (version 5.3.5) [1] is used in association with the BLAS library provided by Intel 17.0.4 MKL, for partial factorization and associated solves (reduction and expansion phases). Eigen library[5] (version 3.3.8) is used for dense linear algebra, for the Singular value decomposition of the Schur complement and for all iterative solvers involved in the computation of centrality measures. The eigenvalues computation needed for the evaluation of condition numbers make use of the ARPACK library through the Python module `scipy.sparse.linalg` and the Z-set Python interface.

## 6.1 Academic thermal 2D examples

This section provides a small academic examples in order to understand the behavior of the various centrality measures proposed. The problem considered is the steady-state heat equation on the unit square without any boundary Dirichlet condition $\Delta u = 0$ (see Figure 4).

The square is made of two different materials with thermal conductivity $\kappa_r$ (resp. $\kappa_b$) for the red (resp. blue) area. Three conductivity ratio will be considered $\kappa_r/\kappa_b \in (10^{-2}, 1, 10^2)$. The unit square is discretized with a $20 \times 20$ Q1 finite elements. The conduction operator arising from the finite element discretization is singular, its nullspace is the constant vector $\boldsymbol{R} = \mathbf{1}_{n_v}$. It corresponds to floating sudomains when the FETI method is used to solve steady-state thermal problems. We use only one fixing-node since the defect is 1.

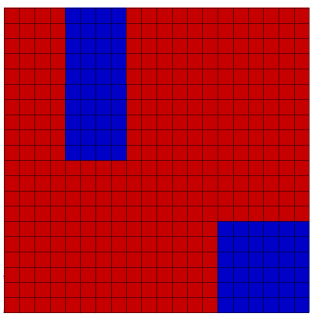

Figure 4: Academic thermal example, the unit square is made of two different material with conductivity $\kappa_r$ and $\kappa_b$.

### 6.1.1 Comparison of all methods

For Katz and PageRank centralities which depend on the parameter $\alpha$, nine values are tested $(0.1, 0.2, 0.3, 0.4, 0.5, 0.6, 0.7, 0.8, 0.9)$. Only the best results, with respect to the value of $\alpha$, are displayed. The best

[3] http://www.zset-software.com/
[4] http://mumps.enseeiht.fr/
[5] http://eigen.tuxfamily.org/

result is marked with an exponent $\square^b$. The influence of the parameter $\alpha$ is discussed in Section 6.1.2. The lumped weight is used in the section.

The results of all methods are shown in Table 1. To visualize the behavior of centrality measures, the normalized score of the Weighted Perron, Katz and PageRank centralities are plotted in Figure 5, 6 and 7.

| $\overline{\text{cond}}(\boldsymbol{\mathcal{A}})$ | 2.04e+03 | |
|---|---|---|
| Strategy | $\text{cond}(\boldsymbol{\mathcal{A}}_{\overline{cc}})$ | $\overline{\text{cond}}(\boldsymbol{\mathcal{A}}^+)$ |
| Mumps | 2.04e+03 | 1.76e+03 |
| Gravity center | **1.10e+03** | **1.10e+03** |
| Perron | **1.10e+03** | **1.10e+03** |
| Katz$^b$ | **1.10e+03** | **1.10e+03** |
| PageRank$^b$ | 2.64e+03 | 2.48e+03 |
| Weighted Perron | **1.10e+03** | **1.10e+03** |
| Weighted Katz$^b$ | **1.10e+03** | **1.11e+03** |
| Weighted PageRank$^b$ | 1.25e+03 | 1.30e+03 |

Results for $\kappa_r/\kappa_b = 10^0$

| $\overline{\text{cond}}(\boldsymbol{\mathcal{A}})$ | 1.82e+06 | |
|---|---|---|
| Strategy | $\text{cond}(\boldsymbol{\mathcal{A}}_{\overline{cc}})$ | $\overline{\text{cond}}(\boldsymbol{\mathcal{A}}^+)$ |
| Mumps | 1.82e+06 | 1.56e+06 |
| Gravity center | 9.47e+05 | 9.56e+05 |
| Perron | 9.47e+05 | 9.56e+05 |
| Katz$^b$ | 9.47e+05 | 9.56e+05 |
| PageRank$^b$ | 6.38e+05 | 6.38e+05 |
| Weighted Perron | 6.37e+05 | 6.37e+05 |
| Weighted Katz$^b$ | 6.37e+05 | 6.37e+05 |
| Weighted PageRank$^b$ | **3.60e+05** | **3.61e+05** |

Results for $\kappa_r/\kappa_b = 10^{-2}$

| $\overline{\text{cond}}(\boldsymbol{\mathcal{A}})$ | 4.35e+03 | |
|---|---|---|
| Strategy | $\text{cond}(\boldsymbol{\mathcal{A}}_{\overline{cc}})$ | $\overline{\text{cond}}(\boldsymbol{\mathcal{A}}^+)$ |
| Mumps | 4.35e+03 | 4.30e+03 |
| Gravity center | 4.21e+03 | 4.22e+03 |
| Perron | 4.21e+03 | 4.22e+03 |
| Katz$^b$ | 4.21e+03 | 4.22e+03 |
| PageRank$^b$ | 4.56e+03 | 4.85e+03 |
| Weighted Perron | 4.21e+03 | 4.22e+03 |
| Weighted Katz$^b$ | **4.20e+03** | **4.21e+03** |
| Weighted PageRank$^b$ | 4.21e+03 | 4.22e+03 |

Results for $\kappa_r/\kappa_b = 10^2$

Table 1: Academic thermal example: comparison of all methods

When $\kappa_r/\kappa_b = 1$, the square is homogeneous and the best fixing-node is the central one which coincides with the gravity center of all mesh nodes. This central node is picked up by almost all methods. Logically, the use of the weighted graph is not useful for this homogeneous problem. An interesting point is that all PageRank variants do not select to the optimal fixing-node here. As illustrated in Figure 5, all interior nodes have the same PageRank centrality and the position of the node has little impact. A similar behavior is seen on the Katz centrality but the map is slightly smoother. For Katz (with $\alpha = 0.5$), the transition between low score frontier nodes to high score interior nodes involves two band of elements. This transition depends on the parameter $\alpha$ and when $\alpha \to 1$, the Katz centrality becomes similar to the Eigenvector centrality.

When $\kappa_r/\kappa_b = 10^2$, the red central part of the square is more conductive than the blue one. The central node remains a good fixing-node candidate and the results are similar to the homogeneous case. As shown in Figure 6,

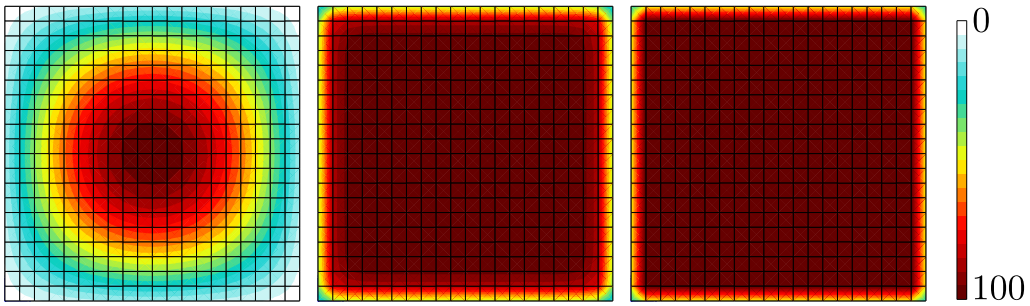


Figure 5: Academic thermal example: centrality map obtained with lumped weights with $\kappa_r = \kappa_b$.

the Eigenvector centrality leads to a small area with high centrality while Katz and PageRank precisely detect the high conductivity areas.

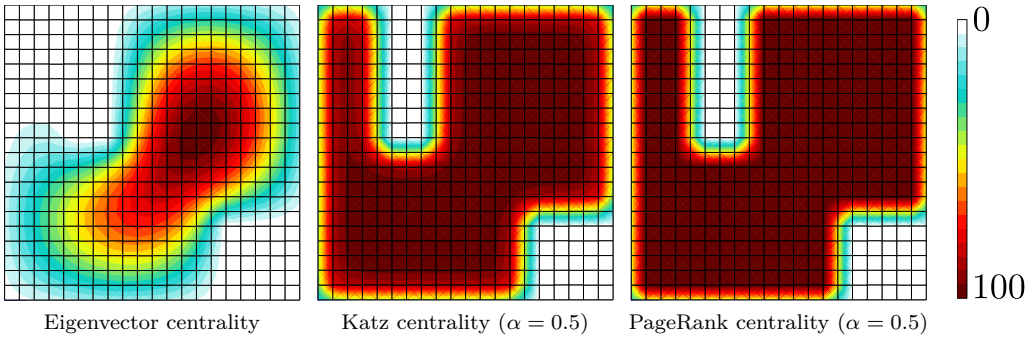


Figure 6: Academic thermal example: centrality map obtained with lumped weights with $\kappa_r/\kappa_b = 10^2$.

The case $\kappa_r/\kappa_b = 10^{-2}$ is more interesting. Here, the red central part of the square is less conductive than the blue one and the central node of the square is not a good fixing-node candidate. Without the use of the weighted graph, Perron, Katz and Gravity center methods still select the central node of the square. By taking into account this heterogeneity, all weighted methods provide a better fixing-node and decrease the condition numbers of both the generalized inverse and of the inner block. Due to the simplicity of the test case, the improvement of the condition number remains limited but the mechanism remains promising. Again, Figure 7 plots the centrality score. Both Katz and PageRank centralities detect the two high conductivity areas while the Eigenvector centrality only got the right lower one.

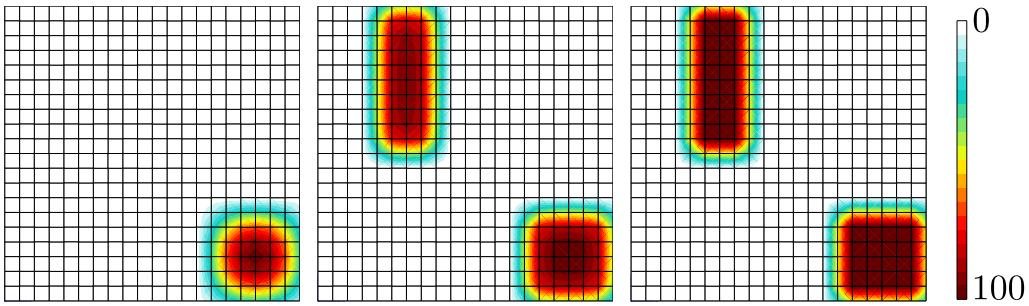


Figure 7: Academic thermal example: centrality map obtained with lumped weights with $\kappa_r/\kappa_b = 10^{-2}$.

### 6.1.2 Influence of the parameter $\alpha$

The influence of the parameter $\alpha$ on the condition number are shown in Table 2 for the Katz centrality and in Table 3 and for the PageRank one. As can be seen in Table 2, the damping parameter $\alpha$ has little impact on the fixing-node selected by the Katz centrality. All $\alpha \geq 0.5$ provide the same fixing-node. Regarding the PageRank centrality in Table 2, results are also clustered but no clear tendency can be drawn. This litte sensitivity may be due to the intrinsic part of the centrality $\boldsymbol{\beta}$ which is defined as the diagonal value of the matrix. It may also be reduced by the simplicity of this test case. This little sensitivity is rather beneficial since a fine tuning of the parameter alpha is not necessary.

| $\overline{\text{cond}}(\boldsymbol{\mathcal{A}})$ | 1.42e+05 | |
|---|---|---|
| $\alpha$ | $\text{cond}(\boldsymbol{\mathcal{A}}_{\overline{cc}})$ | $\overline{\text{cond}}(\boldsymbol{\mathcal{A}}^+)$ |
| 0.1 | 6.37e+05 | 6.37e+05 |
| 0.2 | 6.37e+05 | 6.37e+05 |
| 0.3 | 6.37e+05 | 6.37e+05 |
| 0.4 | 6.37e+05 | 6.37e+05 |
| 0.5 | 6.37e+05 | 6.37e+05 |
| 0.6 | 6.37e+05 | 6.37e+05 |
| 0.7 | 6.37e+05 | 6.37e+05 |
| 0.8 | 6.37e+05 | 6.37e+05 |
| 0.9 | 6.37e+05 | 6.37e+05 |

Results for $\kappa_r/\kappa_b = 10^{-2}$

| $\overline{\text{cond}}(\boldsymbol{\mathcal{A}})$ | 1.87e+02 | |
|---|---|---|
| $\alpha$ | $\text{cond}(\boldsymbol{\mathcal{A}}_{\overline{cc}})$ | $\overline{\text{cond}}(\boldsymbol{\mathcal{A}}^+)$ |
| 0.1 | 1.25e+03 | 1.30e+03 |
| 0.2 | 1.30e+03 | 1.37e+03 |
| 0.3 | 1.25e+03 | 1.30e+03 |
| 0.4 | 1.12e+03 | 1.13e+03 |
| 0.5 | 1.10e+03 | 1.11e+03 |
| 0.6 | 1.10e+03 | 1.10e+03 |
| 0.7 | 1.10e+03 | 1.10e+03 |
| 0.8 | 1.10e+03 | 1.10e+03 |
| 0.9 | 1.10e+03 | 1.10e+03 |

Results for $\kappa_r/\kappa_b = 10^{0}$

| $\overline{\text{cond}}(\boldsymbol{\mathcal{A}})$ | 3.88e+03 | |
|---|---|---|
| $\alpha$ | $\text{cond}(\boldsymbol{\mathcal{A}}_{\overline{cc}})$ | $\overline{\text{cond}}(\boldsymbol{\mathcal{A}}^+)$ |
| 0.1 | 4.20e+03 | 4.21e+03 |
| 0.2 | 4.26e+03 | 4.27e+03 |
| 0.3 | 4.24e+03 | 4.26e+03 |
| 0.4 | 4.24e+03 | 4.26e+03 |
| 0.5 | 4.24e+03 | 4.26e+03 |
| 0.6 | 4.24e+03 | 4.26e+03 |
| 0.7 | 4.24e+03 | 4.26e+03 |
| 0.8 | 4.23e+03 | 4.24e+03 |
| 0.9 | 4.23e+03 | 4.24e+03 |

Results for $\kappa_r/\kappa_b = 10^{2}$

Table 2: Academic thermal example: influence of the parameter $\alpha$ for Weighted Katz

## 6.2 Solid benchmark

This Section provides a 3D elasto-static example. It is a generalization of the solid benchmark proposed in [11]. First the unit cube is discretized using a $6 \times 6 \times 6$ regular grid made with Q1 elements (c3d8). Then this unit cube is

| $\overline{\text{cond}}(\boldsymbol{\mathcal{A}})$ | 1.42e+05 | |
|---|---|---|
| $\alpha$ | $\text{cond}(\boldsymbol{\mathcal{A}}_{\overline{cc}})$ | $\overline{\text{cond}}(\boldsymbol{\mathcal{A}}^{+})$ |
| 0.1 | 3.60e+05 | 3.61e+05 |
| 0.2 | 3.61e+05 | 3.61e+05 |
| 0.3 | 3.61e+05 | 3.61e+05 |
| 0.4 | 3.63e+05 | 3.64e+05 |
| 0.5 | 3.60e+05 | 3.61e+05 |
| 0.6 | 3.62e+05 | 3.62e+05 |
| 0.7 | 3.62e+05 | 3.63e+05 |
| 0.8 | 3.61e+05 | 3.61e+05 |
| 0.9 | 3.61e+05 | 3.61e+05 |

Results for $\kappa_r/\kappa_b = 10^{-2}$

| $\overline{\text{cond}}(\boldsymbol{\mathcal{A}})$ | 1.87e+02 | |
|---|---|---|
| $\alpha$ | $\text{cond}(\boldsymbol{\mathcal{A}}_{\overline{cc}})$ | $\overline{\text{cond}}(\boldsymbol{\mathcal{A}}^{+})$ |
| 0.1 | 1.37e+03 | 1.45e+03 |
| 0.2 | 1.30e+03 | 1.37e+03 |
| 0.3 | 1.89e+03 | 3.14e+03 |
| 0.4 | 1.89e+03 | 2.54e+03 |
| 0.5 | 1.69e+03 | 1.51e+03 |
| 0.6 | 1.25e+03 | 1.30e+03 |
| 0.7 | 1.78e+03 | 1.92e+03 |
| 0.8 | 1.69e+03 | 1.51e+03 |
| 0.9 | 1.81e+03 | 2.33e+03 |

Results for $\kappa_r/\kappa_b = 10^{0}$

| $\overline{\text{cond}}(\boldsymbol{\mathcal{A}})$ | 3.88e+03 | |
|---|---|---|
| $\alpha$ | $\text{cond}(\boldsymbol{\mathcal{A}}_{\overline{cc}})$ | $\overline{\text{cond}}(\boldsymbol{\mathcal{A}}^{+})$ |
| 0.1 | 4.56e+03 | 4.85e+03 |
| 0.2 | 4.27e+03 | 4.29e+03 |
| 0.3 | 4.56e+03 | 4.85e+03 |
| 0.4 | 4.21e+03 | 4.22e+03 |
| 0.5 | 4.56e+03 | 4.85e+03 |
| 0.6 | 4.56e+03 | 4.85e+03 |
| 0.7 | 4.91e+03 | 5.10e+03 |
| 0.8 | 4.56e+03 | 4.85e+03 |
| 0.9 | 4.56e+03 | 4.85e+03 |

Results for $\kappa_r/\kappa_b = 10^{2}$

Table 3: Academic thermal example: influence of the parameter $\alpha$ for Weighted PageRank

deformed using the map $f$

$$f : \begin{cases} [0,1]^3 & \to \mathbb{R}^3 \\ (x,y,z) & \mapsto \left((x-\frac{1}{2}) \times (1-0.6\sqrt{z}),\ (y-\frac{1}{2}) \times (1-0.6\sqrt{z}), \sqrt{z}\right) \end{cases}$$

.

As shown in Figure 8, the unit cube becomes a truncated pyramid. This truncated pyramid is made of two different materials. Both layers share the same Poisson's coefficient 0.3 but the Young's modulus alternates between a soft value $E_r$ and a stiff one $E_b$. Three values of heterogeneity ratio are considered $E_b/E_r \in \{1, 10^2, 10^3\}$. The truncated pyramid is totally floating, the defect of the associated stiffness matrix is 6. Only four condensation nodes are used in this benchmark, leading to a Schur complement $\boldsymbol{S}_{cc}$ of size $12 \times 12$.

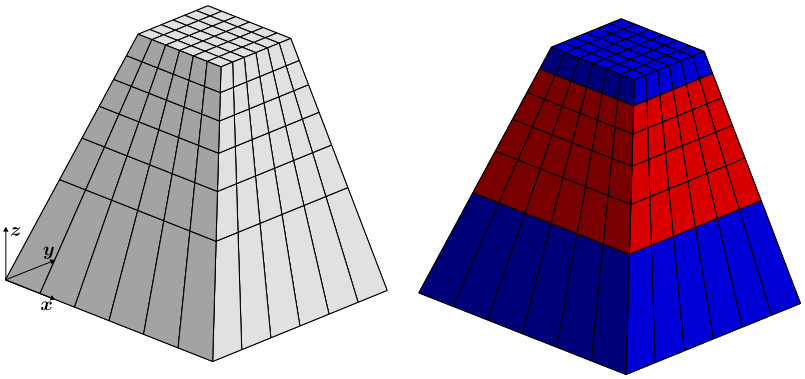


Figure 8: Solid benchmark: the solid is made of two different material with Young modulus $E_r$ and $E_b$. Inspired by [11]

Again, all proposed methods are compared and results are gathered in Table 4. For Katz and PageRank centralities which depend on the parameter $\alpha$, nine values are tested $(0.1, 0.2, 0.3, 0.4, 0.5, 0.6, 0.7, 0.8, 0.9)$. Only the best and

worst results, with respect to the value of $\alpha$, are displayed. The best result (resp. worst) is marked with an exponent $\square^b$ (resp. $\square^w$).

As shown in Table 4, weighted variants perform better than unweighted ones. For the homogeneous case case ($E_b = E_r$), all results are clustered. For heterogeneous problem, the weighted variants lead to a reduction of the condition number of a factor $10^2$ in comparison with Mumps. The condition number is approximately reduced by a factor 10 if we compare with gravity center method or unweighted centralities. The sensitivity to the parameter $\alpha$ is again reduced since best and worst results are similar.

| $\overline{\text{cond}}(\boldsymbol{\mathcal{A}})$ | 7.82e+04 | |
|---|---|---|
| Strategy | $\text{cond}(\boldsymbol{\mathcal{A}}_{\overline{cc}})$ | $\overline{\text{cond}}(\boldsymbol{\mathcal{A}}^+)$ |
| Mumps | 7.82e+04 | 7.79e+04 |
| Gravity center | 3.81e+03 | 3.08e+03 |
| Perron | 4.52e+03 | 4.48e+03 |
| Katz$^b$ | 4.52e+03 | 4.48e+03 |
| Katz$^w$ | 4.52e+03 | 4.48e+03 |
| PageRank$^b$ | 4.31e+03 | 4.22e+03 |
| PageRank$^w$ | 4.60e+04 | 4.35e+04 |
| Weighted Perron | **2.86e+03** | **2.67e+03** |
| Weighted Katz$^b$ | **2.86e+03** | **2.67e+03** |
| Weighted Katz$^w$ | 4.58e+03 | 4.49e+03 |
| Weighted PageRank$^b$ | 5.64e+03 | 5.50e+03 |
| Weighted PageRank$^w$ | 6.74e+03 | 6.68e+03 |

Results for $E_b = E_r$

| $\overline{\text{cond}}(\boldsymbol{\mathcal{A}})$ | 6.52e+06 | |
|---|---|---|
| Strategy | $\text{cond}(\boldsymbol{\mathcal{A}}_{\overline{cc}})$ | $\overline{\text{cond}}(\boldsymbol{\mathcal{A}}^+)$ |
| Mumps | 6.52e+06 | 5.96e+06 |
| Gravity center | 1.52e+05 | 5.05e+04 |
| Perron | 2.73e+05 | 2.49e+05 |
| Katz$^b$ | 2.73e+05 | 2.49e+05 |
| Katz$^w$ | 2.73e+05 | 2.49e+05 |
| PageRank$^b$ | 9.17e+04 | 6.39e+04 |
| PageRank$^w$ | 3.19e+05 | 2.97e+05 |
| Weighted Perron | **3.46e+04** | **3.09e+04** |
| Weighted Katz$^b$ | **3.46e+04** | **3.09e+04** |
| Weighted Katz$^w$ | 3.96e+04 | 3.14e+04 |
| Weighted PageRank$^b$ | 5.16e+04 | 3.27e+04 |
| Weighted PageRank$^w$ | 8.70e+04 | 4.76e+04 |

Results for $E_b/E_r = 10^2$

| $\overline{\text{cond}}(\boldsymbol{\mathcal{A}})$ | 6.56e+07 | |
|---|---|---|
| Strategy | $\text{cond}(\boldsymbol{\mathcal{A}}_{\overline{cc}})$ | $\overline{\text{cond}}(\boldsymbol{\mathcal{A}}^+)$ |
| Mumps | 6.56e+07 | 5.93e+07 |
| Gravity center | 1.49e+06 | 4.80e+05 |
| Perron | 2.70e+06 | 2.44e+06 |
| Katz$^b$ | 2.70e+06 | 2.44e+06 |
| Katz$^w$ | 2.70e+06 | 2.44e+06 |
| PageRank$^b$ | 8.82e+05 | 5.47e+05 |
| PageRank$^w$ | 2.49e+06 | 2.21e+06 |
| Weighted Perron | **3.42e+05** | **2.94e+05** |
| Weighted Katz$^b$ | **3.42e+05** | **2.94e+05** |
| Weighted Katz$^w$ | 3.88e+05 | 2.92e+05 |
| Weighted PageRank$^b$ | 4.99e+05 | 2.88e+05 |
| Weighted PageRank$^w$ | 8.31e+05 | 3.99e+05 |

Results for $E_b/E_r = 10^3$

Table 4: Solid benchmark: comparison of all methods. For Katz and PageRank only the best and worst results are shown.

### 6.3 Robustness of the kernel detection process on a simplified laminated composite

All kernel detection methods rely on thresholds which may be automatically chosen or provided by the user. The larger is the admissible range, leading to a correct estimation of the kernel dimension, the more robust is the method. As pointed out in [15], the admissible range becomes narrow when considering ill conditioned systems. It is possible to put in difficulty most advanced direct solvers such as MUMPS with pathological test cases. In this section, we provide such a test case and demonstrate the robustness of proposed methods.

A slender heterogeneous (3D) plate with aspect ratio $20 \times 10 \times 1$ discretized into $100 \times 50 \times 10$ regular twenty-node brick elements (c3d20) (see Figure 9). The surface $x = 0$ is clamped and a pressure is prescribed at the surface $x = 20$. This plate is made of five thin linear elastic layers (see Fig. 9a). All layers share the same Poisson's coefficient 0.3 but the Young's modulus alternates between a soft value $E_r$ and a stiff one $E_b$. This case aims at representing a laminated composite material made out of a soft material reinforced by a stiffer one. Six values of heterogeneity ratio are considered $E_b/E_r \in \{10^2, 10^3, 10^4, 10^5, 10^6\}$.

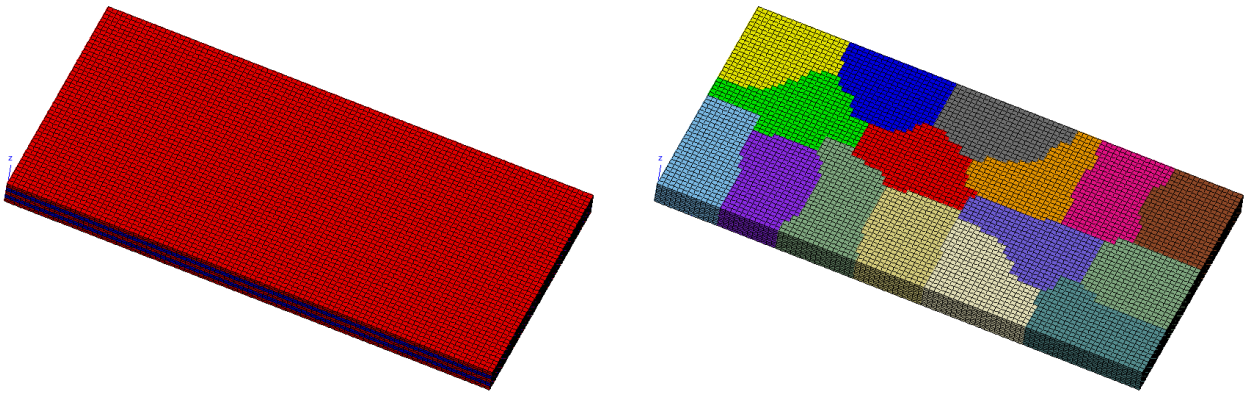

Soft material is in red, stiff material in blue. Automatic decomposition with 16 subdomains.

Figure 9: Heterogeneous composite.

In order to solve the problem with AMPFETI [4], the mesh is split into 16 domains (see Figure 9b) composed on average of 3100 elements and contains 45000 degrees of freedom. With this decomposition, there is only one subdomain in the thickness. Fourteen subdomains are totally floating, the defect of the corresponding local stiffness operators is six. Also, stiffness operators are ill conditioned due to the bad subdomain aspect ratio and the jump of material coefficient.

### 6.3.1 Kernel detection with MUMPS 5.3.5

There are two user defined parameters, CNTL(1) and CNTL(3), for the detection of the kernel dimension in MUMPS 5.3.5. The control parameter CNTL(1) is a relative threshold for numerical pivoting. The default value CNTL(1) = 1e-2 is used in this work. The second control parameter CNTL(3) is a threshold to detect null pivots. According to the documentation, a pivot is considered to be null if the infinite norm of its row/column is smaller than a threshold *thres*. The default value of CNTL(3) = 0 provides an automatic process to determines this threshold, $thres = \epsilon \times 10^{-5} \times ||A_{pre}||$ where $A_{pre}$ is the preprocessed matrix to be factorized and $\epsilon$ is machine precision. A positive value of CNTL(3) leads to the user defined threshold $thres = CNTL(3) \times ||A_{pre}||$.

The result of the kernel detection procedure for totally unrestrained subdomain is shown in Table 5. The exact kernel dimension is 6. Whatever the heterogeneity, the automatic threshold does not detect the right kernel size. With a user defined threshold, it is possible to recover the right kernel one. However, the admissible range for CNTL(3) decreases when considering high heterogeneity. The validity range for the case $E_b/E_r = 1e{+}6$ is less than two decades.

| $E_b/E_r$ | threshold for null pivots by CNTL(3) | | | | | | |
|---|---|---|---|---|---|---|---|
| | 1e-03 | 1e-04 | 1e-05 | 1e-06 | 1e-07 | 1e-08 | automatic |
| 1e+02 | **6** | **6** | **6** | **6** | **6** | **6** | 0 |
| 1e+03 | **6** | **6** | **6** | **6** | **6** | 5 | 0 |
| 1e+04 | **6** | **6** | **6** | **6** | 4 | 3 | 0 |
| 1e+05 | 7 | **6** | **6** | 5 | 5 | 3 | 0 |
| 1e+06 | 9 | **6** | 5 | 4 | 3 | 3 | 0 |

Table 5: Laminated composite: dependency of kernel detection on a parameter in MUMPS. It corresponds to the red subdomain in Figure 9.

### 6.3.2 Graph based methods

The graph based kernel detection methods are applied to the same totally unrestrained subdomain. In order to highlight the robustness of the proposed methods, the singular values of the Schur complement selected by the Katz and Page Rank are shown in Figure 10. The validity range of the threshold $\epsilon$ for the Relative criterion (11) and Jump criterion (12) can be obtained with this graph. The lumped weight is used for both methods and three damping values are considered $\alpha \in (0.3, 0.5, 0.9)$. Only four condensation nodes are used in this benchmark, leading to a Schur complement $\boldsymbol{S}_{cc}$ of size $12 \times 12$. As shown in Figure 10, whatever the heterogeneity ratio $E_b/E_r$, the singular values associated with the six rigid body motions are easily recognizable. For all cases, the admissible range for the selection threshold covers at least five decades.

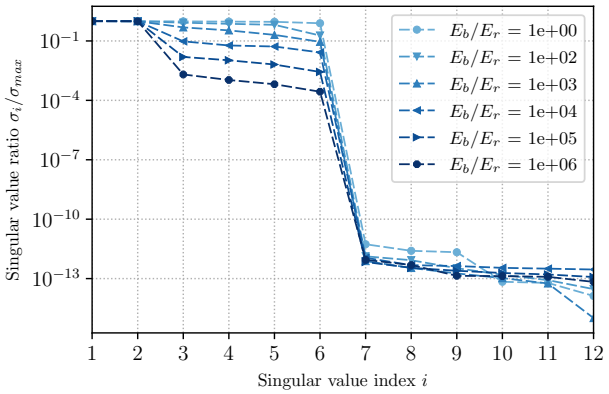


Katz with damping parameter $\alpha = 0.3$.

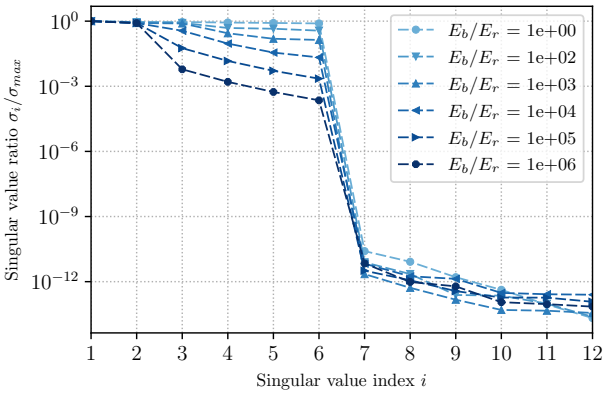


Page Rank with damping parameter $\alpha = 0.3$.

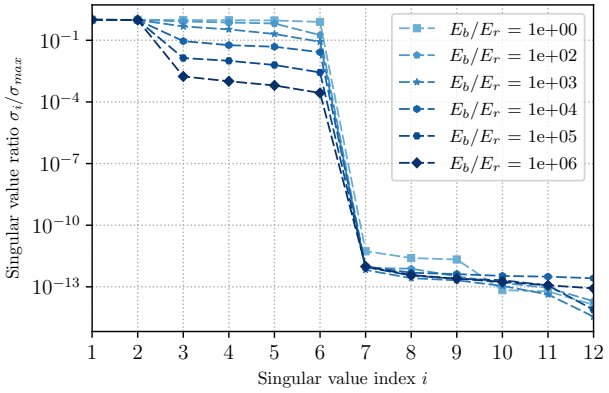


Katz with damping parameter $\alpha = 0.5$.

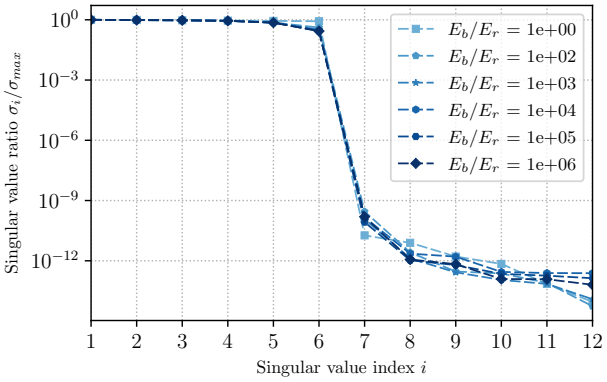


Page Rank with damping parameter $\alpha = 0.5$.

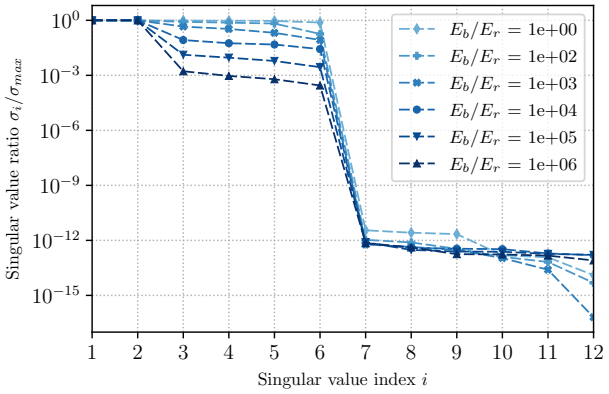


Katz with damping parameter $\alpha = 0.9$.

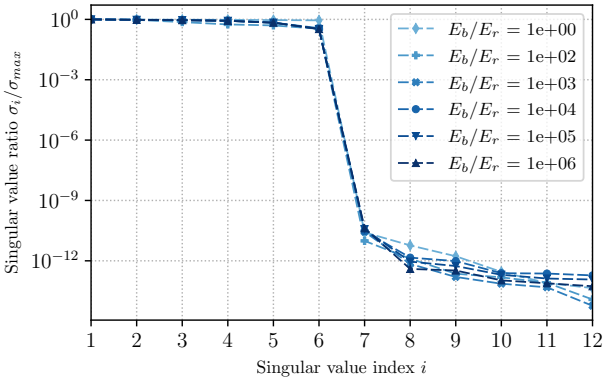


Page Rank with damping parameter $\alpha = 0.9$.

Figure 10: Laminated composite: singular values of the Schur complement $\boldsymbol{S}_{cc}$ for Katz and Page Rank. Four condensation nodes are used with lumped weight.

# 7 Application to engineering problems: numerical homogenization of the mechanical behavior of solid propellants

Solid propellants are energetic materials composed of an organic matrix and numerous metallic inclusions. This type of material brings several space scales into play because of the large dispersion of the particles sizes. The numerical homogenization of this type of material involves the simulation of a Representative Volume Element (RVE) with a large number of unknowns. Iterative solvers are essential whereas they are put to the test by the condition number of the linear systems.

Indeed, the material is highly heterogeneous, the jump in Young modulus between the matrix and the metallic inclusions is approximately $10^5$. Because of the high density of inclusions in the RVE, heterogeneity is very frequently misplaced with respect to the domain decomposition interface. Also, elements of the mesh of the matrix that are located between two close inclusions often exhibit poor quality factors which degrade even more the condition number of the linear system to be solved. Finally, the organic matrix is almost incompressible. If a linear elastic behavior is assumed for the matrix, the Poisson coefficient is 0.499 such that mixed pressure–displacement–volume variation finite element needs to be used (see Section 2.6 and Section 5.5 in [45]). For simplicity, the geometrically linearized problem is considered. This assumption has little impact on the conclusion of the study. In the case of the finite strain model, the kernel detection and generalized inverse computation are applied to the tangent system.

Domain decomposition methods, such as the FETI method and its derivatives do not escape from these difficulties. The interface iterative solver needs some special care, this is a typical case where AMPFETI is needed. A robust process to detect local operators nullspaces and to compute generalized inverse is also essential. Figure 11a shows results obtained in a previous work [5]. The finite element mesh and the domain decomposition for one distribution of particles. The finite element mesh contains 5,494,528 quadratic tetrahedrons and the global system has 22 millions of degrees of freedom; 448 subdomains are used for the partitioning. The RVE is submitted to hydrostatic compression. The Von Mises stress field is shown in 11c for a hydrostatic compression load. The focus is carried on the two typical subdomains shown in Figure 12. The first one is in the bulk of the RVE. This subdomain is totally floating and possesses six rigid body motions. The second one is close to a boundary. Under hydrostatic compression, only the normal displacement of the external surface of the RVE is constrained. So, this subdomain is partially constrained and posses only three rigid body motions.

### 7.0.1 Short recall of three field mixed elements

This section quickly recall the theory of three field mixed elements, more details can be found for example in Section 2.6 and Section 5.5 in [45]. The treatment of nearly incompressible materials is considered by splitting the

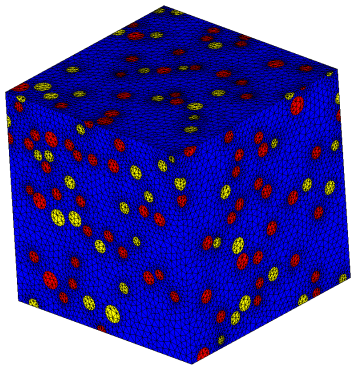

Finite element mesh of the RVE, the red and yellow colors correspond to two different types of inclusions.

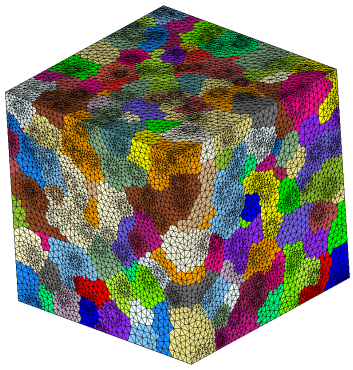

Domain decomposition in 448 subdomains.

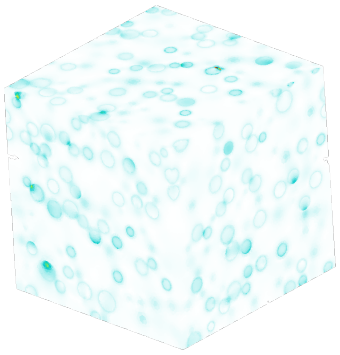

Von Mises stress field, the white color characterises low stresses area.

Figure 11: Numerical homogenization of the mechanical behavior of solid propellants.

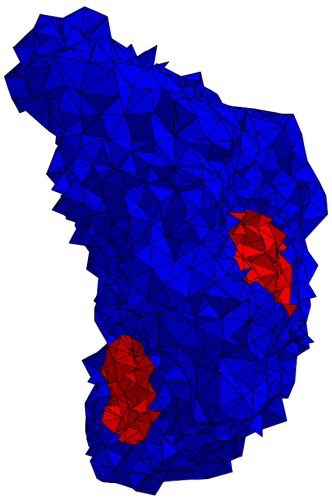

Typical aspect of a subdomain in the bulk of the RVE. This subdomain is totally unrestrained.

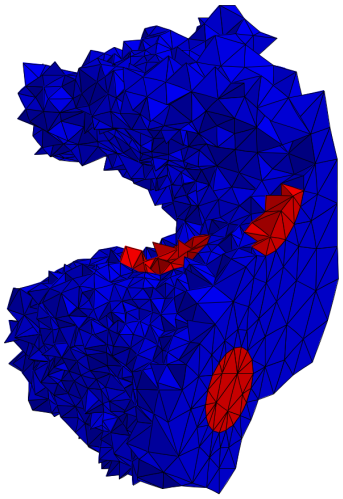

Typical aspect of a subdomain close to a boundary. This subdomain is partially constrained by the boundary condition (hydrostatic compression).

Figure 12: Solid propellants: typical aspect of subdomain meshes.

stress and strain into their deviatoric and sperical parts. The linearized strain $\boldsymbol{\varepsilon}$ is expressed in the mixed form

$$\boldsymbol{\varepsilon} = \boldsymbol{I}_{dev} : \nabla^s \boldsymbol{u} + \frac{1}{3}\theta \mathbf{1} \tag{17}$$

where $\boldsymbol{u}$ is the displacement and $\theta$ is the volume variation. Classically, $\nabla^s \boldsymbol{u}$ is the symmetrized displacement gradient and $\mathbf{1}$ is the second order identify tensor. The fourth-order tensor $\boldsymbol{I}_{dev}$ is a projection operator mapping a symmetric

second-order tensor into its deviatoric part, such that $\boldsymbol{I}_{dev} \colon \nabla^s \boldsymbol{u} = \nabla^s \boldsymbol{u} - \frac{1}{3}\,\mathrm{trace}(\nabla^s \boldsymbol{u})\mathbf{1}$. Similarly the fourth-order tensor $\boldsymbol{I}_{vol}$ is defined, it maps a symmetric second-order tensor into its volumetric part, such that $\boldsymbol{I}_{vol} \colon \nabla^s \boldsymbol{u} = \frac{1}{3}\,\mathrm{trace}(\nabla^s \boldsymbol{u})\mathbf{1}$. The stresses are also expressed in a mixed form as

$$\boldsymbol{\sigma} = \boldsymbol{I}_{dev} \colon \bar{\boldsymbol{\sigma}} + p\mathbf{1} \tag{18}$$

where $p$ is the pressure and $\bar{\boldsymbol{\sigma}}$ is the stresses deduced from the constitutive model $\bar{\boldsymbol{\sigma}} = \boldsymbol{\sigma}(\boldsymbol{\varepsilon})$. Assuming quasi-static problem, the weak form is given by

$$\begin{aligned} \int_\Omega \delta\nabla^s \boldsymbol{u} \colon \boldsymbol{\sigma}\; d\Omega &= \int_\Omega \delta\boldsymbol{u} \cdot \boldsymbol{b}\; d\Omega + \int_{\partial\Omega} \delta\boldsymbol{u} \cdot \boldsymbol{t}\; d\Gamma \\ \int_\Omega \delta p\,(\boldsymbol{I}_{vol} \colon \nabla^s \boldsymbol{u} - \theta)\;\; d\Omega &= 0 \\ \int_\Omega \delta\theta\,(\boldsymbol{I}_{vol} \colon \bar{\boldsymbol{\sigma}} - p)\;\; d\Omega &= 0 \end{aligned} \tag{19}$$

where $\boldsymbol{b}$ and $\boldsymbol{t}$ are body and traction forces, respectively. The virtual quantities are denoted $\delta\boldsymbol{u}, \delta p$ and $\delta\theta$. The finite element approximations are given by $\boldsymbol{u} \approx \boldsymbol{N}_u\,\{\boldsymbol{u}\}$, $p \approx \boldsymbol{N}_p\,\{\boldsymbol{p}\}$ and $\theta \approx \boldsymbol{N}_\theta\,\{\boldsymbol{\theta}\}$. The same approximations is chosen for the virtual quantities. The Voigt notation for the strain and stresses tensors are denoted, $\{\boldsymbol{\varepsilon}\}$ and $\{\boldsymbol{\sigma}\}$. With the notation $\boldsymbol{m} = \{1\ 1\ 1\ 0\ 0\ 0\}^\top$, the matrix form of the deviatoric project is $\boldsymbol{I}_d = \boldsymbol{I} - \frac{1}{3}\boldsymbol{m}\boldsymbol{m}^\top$ . The strain and stressses are given by

$$\begin{aligned} \{\boldsymbol{\varepsilon}\} &= \boldsymbol{I}_d \boldsymbol{B}\,\{\boldsymbol{u}\} + \frac{1}{3}\boldsymbol{m}\boldsymbol{N}_\theta\,\{\boldsymbol{\theta}\} \\ \{\boldsymbol{\sigma}\} &= \boldsymbol{I}_d\,\{\bar{\boldsymbol{\sigma}}\} + \boldsymbol{m}\boldsymbol{N}_p\,\{\boldsymbol{p}\} \end{aligned} \tag{20}$$

where $\boldsymbol{B}$ is the standard strain-displacement matrix. In order to obtain the tangent system, the constitutive equation is linearized

$$\{d\bar{\boldsymbol{\sigma}}\} = \boldsymbol{D}_T\,\{d\boldsymbol{\varepsilon}\} \tag{21}$$

where $\{d\boldsymbol{\varepsilon}\}$ is the mixed strain variation and $\boldsymbol{D}_T$ is the tangent modulus. Finally, the tangent system is obtained

$$\boldsymbol{K}^{\boldsymbol{u}p\theta} = \begin{bmatrix} \boldsymbol{K}_{\boldsymbol{u}\boldsymbol{u}} & \boldsymbol{K}_{\boldsymbol{u}\theta} & \boldsymbol{K}_{\boldsymbol{u}p} \\ \boldsymbol{K}_{\theta\boldsymbol{u}} & \boldsymbol{K}_{\theta\theta} & -\boldsymbol{K}_{\theta p} \\ \boldsymbol{K}_{p\boldsymbol{u}} & -\boldsymbol{K}_{p\theta} & \mathbf{0} \end{bmatrix} \tag{22}$$

with

$$\begin{aligned} \boldsymbol{K}_{\boldsymbol{uu}} &= \int_{\Omega} \boldsymbol{B}^{\top} \bar{\boldsymbol{D}}_{11} \boldsymbol{B} d\Omega & \boldsymbol{K}_{\theta p} &= \int_{\Omega} \boldsymbol{N}_{\theta}^{\top} \boldsymbol{N}_{p} d\Omega = \boldsymbol{K}_{p\theta}^{\top} \\ \boldsymbol{K}_{\theta\theta} &= \int_{\Omega} \boldsymbol{N}_{\theta}^{\top} \bar{\boldsymbol{D}}_{22} \boldsymbol{N}_{\theta} d\Omega & \boldsymbol{K}_{p\boldsymbol{u}} &= \int_{\Omega} \boldsymbol{N}_{p}^{\top} \boldsymbol{m}^{\top} \boldsymbol{B} d\Omega = \boldsymbol{K}_{\boldsymbol{u}p}^{\top} \\ & & \boldsymbol{K}_{\theta\boldsymbol{u}} &= \int_{\Omega} \boldsymbol{N}_{\theta}^{\top} \bar{\boldsymbol{D}}_{21} \boldsymbol{B} d\Omega = \boldsymbol{K}_{\boldsymbol{u}\theta}^{\top} \end{aligned} \tag{23}$$

In (23), the modified constitutive tangent matrix are used to be expressed with respect to $d\boldsymbol{u}$ and $d\theta$

$$\begin{aligned} \bar{\boldsymbol{D}}_{11} &= \boldsymbol{I}_d \boldsymbol{D}_T \boldsymbol{I}_d & \bar{\boldsymbol{D}}_{12} &= \boldsymbol{I}_d \boldsymbol{D}_T (\frac{1}{3}\boldsymbol{m}) \\ \bar{\boldsymbol{D}}_{22} &= (\frac{1}{3}\boldsymbol{m}^{\top}) \boldsymbol{D}_T (\frac{1}{3}\boldsymbol{m}) & \bar{\boldsymbol{D}}_{21} &= (\frac{1}{3}\boldsymbol{m}^{\top}) \boldsymbol{D}_T \boldsymbol{I}_d \end{aligned} \tag{24}$$

The choice of the interpolation for $\boldsymbol{u}, p, \theta$ is constrained by the LBB-conditions [7]. In the following, we consider only two types of tetrahedral elements, the first one, denoted P2P0P0 uses a continuous quadratic interpolation for $\boldsymbol{u}$ and piecewise constant interpolation for $p$ and $\theta$. The second one, denoted P2P1P1 emploies a continuous quadratic interpolation for $\boldsymbol{u}$ and linear continuous interpolation for $p$ and $\theta$.

### 7.0.2 Results with P2P0P0 elements

With P2P0P0 elements, the pressure and volume variation are taken locally in each element and since $\boldsymbol{N}_p = \boldsymbol{N}_\theta$, $\boldsymbol{K}_{p\theta}$ is symmetric positve definite. Both $p$ and $\theta$ can be eliminated by static condensation. The modified stiffness matrix $\tilde{\boldsymbol{K}}^{\boldsymbol{u}}$ is symmetric positive definite but remains ill conditioned.

$$\tilde{\boldsymbol{K}}^{\boldsymbol{u}} = \left(\boldsymbol{K}_{\boldsymbol{uu}} - \boldsymbol{K}_{\boldsymbol{u}\theta} \boldsymbol{K}_{\theta\theta}^{-1} \boldsymbol{K}_{\theta\boldsymbol{u}}\right) + \left(\boldsymbol{K}_{\boldsymbol{u}p} + \boldsymbol{K}_{\boldsymbol{u}\theta} \boldsymbol{K}_{\theta\theta}^{-1} \boldsymbol{K}_{\theta p}\right) \left(\boldsymbol{K}_{p\theta} \boldsymbol{K}_{\theta\theta}^{-1} \boldsymbol{K}_{\theta p}\right)^{-1} \left(\boldsymbol{K}_{p\boldsymbol{u}} + \boldsymbol{K}_{p\theta} \boldsymbol{K}_{\theta\theta}^{-1} \boldsymbol{K}_{\theta\boldsymbol{u}}\right) \tag{25}$$

The graph based kernel detection methods are applied to the subdomains shown in Figure 12. The lumped weight is used for both methods and three damping values are considered $\alpha \in (0.3, 0.5, 0.9)$. Only four condensation nodes are used in this benchmark, leading to Schur complements $\boldsymbol{S}_{cc}$ of size $12 \times 12$. The singular values of the Schur complement selected by the weighted Katz and Page Rank strategies are shown in Figure 13. For both methods and whatever the damping values considered, the six null singular values are easily recognizable for the totally floating subdomain. For the partially constrained subdomain, a uniform normal displacement is prescribed on the external surface of the RVE. Three rigid body motions are possible corresponding to a planar motion (two translations and

one rotation in the plane of the external surface). The three null singular values corresponding to these three rigid body motions are also well clustered.

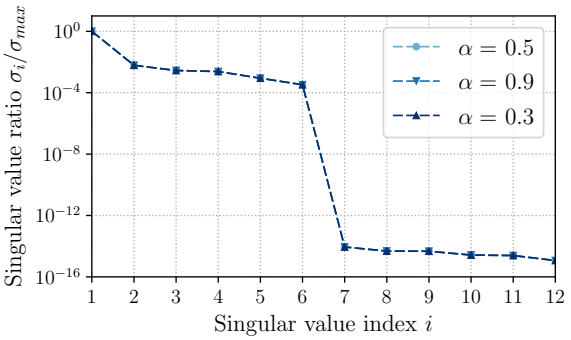


Katz method for a floating subdomain (exact kernel size is 6).

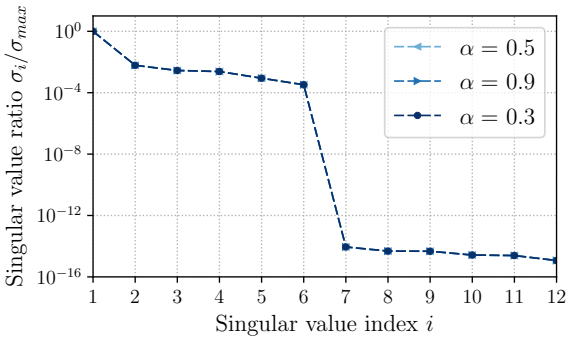


Page Rank method for a floating subdomain (exact kernel size is 6).

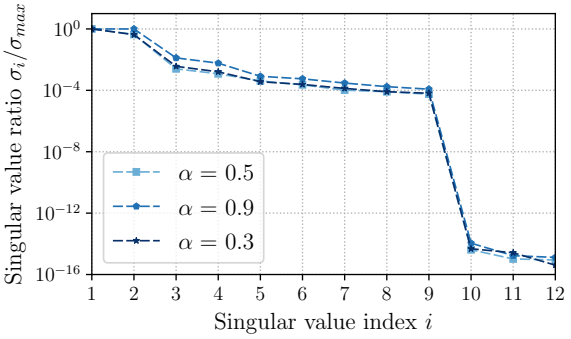


Katz method for a partially floating subdomain (exact kernel size is 3).

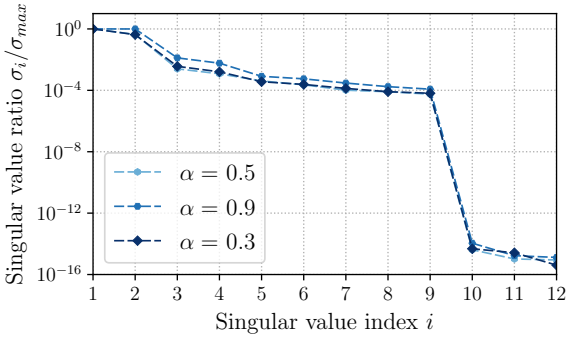


Page Rank method for a partially floating subdomain (exact kernel size is 3).

Figure 13: Solid propellant with P2P0P0 elements : singular values of the Schur complement $\boldsymbol{S}_{cc}$ for Katz and Page Rank. Four condensation nodes are used with lumped weight.

### 7.0.3 Results with P2P1P1 elements

Here, the displacement is interpolated with quadratic shape functions while the pressure and volumic change are continuous and interpolated with linear shape functions. This approximation leads to a symmetric highly indefinite stiffness operator. For such problems, the difference between singular values associated to null eigenvalues and small negative ones becomes unclear without specific strategy. In order to highlight the efficiency of the approach presented in Section 5.3 we compare the singular values of the Schur complement with and without filtering mixed degrees of freedom from the condensation variables.

The graph based kernel detection methods are applied to the subdomains shown in Figure 12. The lumped weight is used for both methods and three damping values are considered $\alpha \in (0.3, 0.5, 0.9)$. Only four condensation nodes are used in this benchmark, leading to Schur complements $\boldsymbol{S}_{cc}$ of size $20 \times 20$ when mixed degrees of freedom are not filtered out, and $12 \times 12$ otherwise.

The singular values of the Schur complement selected by the Katz and Page Rank strategies applied to the floating subdomain are shown in Figure 14. Please note that in order to know in advance the inertia of the Schur complement, both the matrix and the inclusions are discretized with P2P1P1 elements. Pressure and volume discontinuities at the material interface are allowed. It is not a limitation of the method but it facilitates the analysis of the singular values. The inertia of the Schur complement is known *a priori* thanks to the Haynsworth additivity formula. When mixed degrees of freedom are not filtered out, 6 null eigenvalues and 4 (small) negative ones are expected. For both selection strategies, the detection process tends to identify 10 null singular values. The difference between singular values associated to null eigenvalues and small negative ones is totally blurred.

On the contrary, when mixed degrees of freedom are filtered out from the condensation variables, the positivity of the Schur complement is enforced and a clear distinction of null singular values is recovered.

The singular values of the Schur complement selected by the Katz and Page Rank strategies applied to the partially constrained subdomain are shown in Figure 15. Due to the boundary condition, 3 null eigenvalues are expected. Again, the filtering process of mixed degrees of freedom leads to a clear distinction of null singular values.

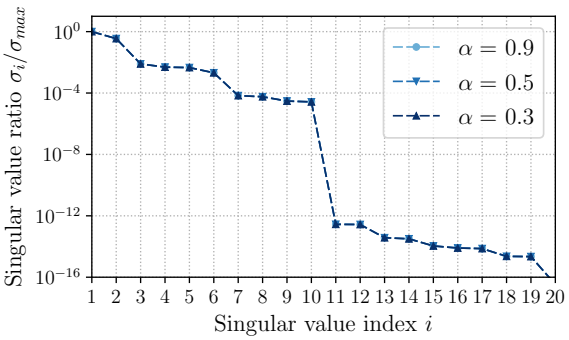


Katz method for a floating subdomain.

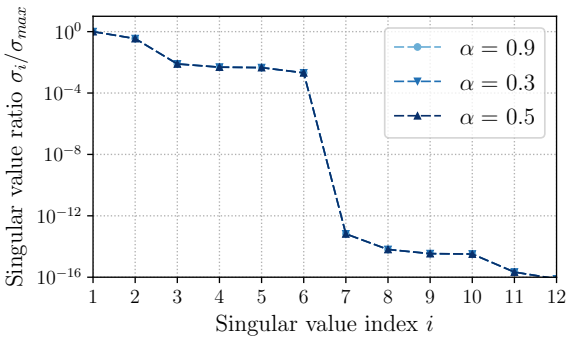


Katz method with mixed dof filter for a floating subdomain.

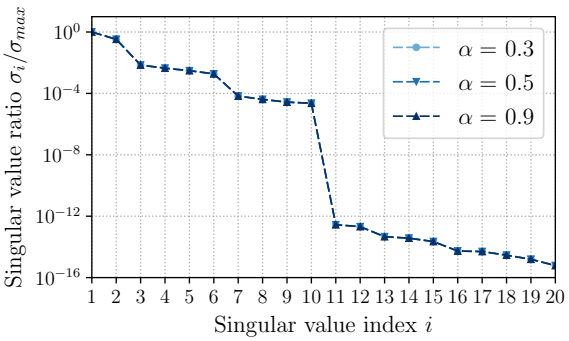


Page Rank method for a floating subdomain.

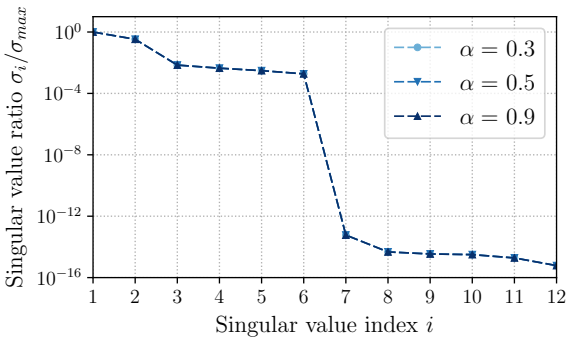


Page Rank method with mixed dof filter for a floating subdomain.

Figure 14: Solid propellant with P2P1P1 elements: singular values of the Schur complement $\boldsymbol{S}_{cc}$ for Katz and Page Rank. Four condensation nodes are used with lumped weight.

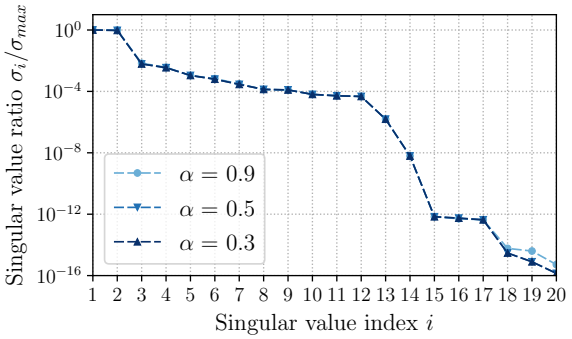


Katz method for a partially constrained subdomain.

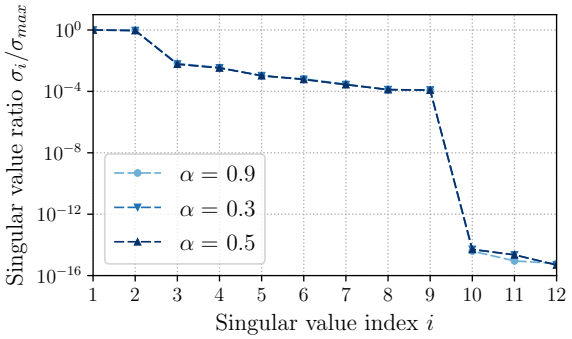


Katz method with mixed dof filter for a partially constrained subdomain.

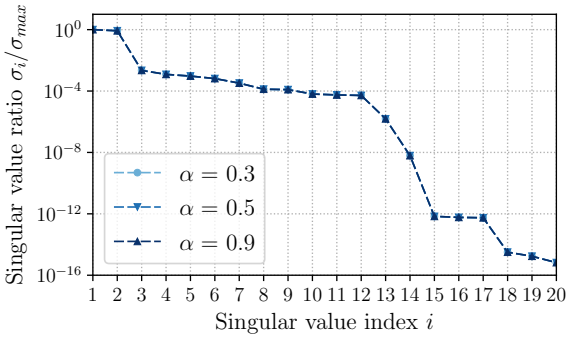


Page Rank method for a partially constrained subdomain.

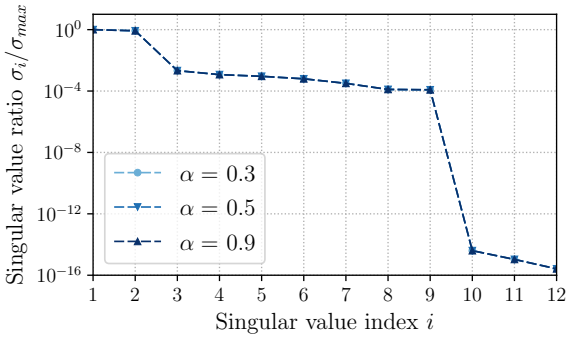


Page Rank method with mixed dof filter for a partially constrained subdomain.

Figure 15: Solid propellant with P2P1P1 elements: singular values of the Schur complement $\boldsymbol{S}_{cc}$ for Katz and Page Rank. Four condensation nodes are used with lumped weight.

# 8 Conclusions

This article has introduced a robust and affordable method to compute nullspace and generalized inverse of finite element operators involved in dual domain decomposition methods. It is a crucial point of the FETI methods since a misdetection of these kernels leads inevitably to the divergence of the iterative solver.

The methodology follows the fixing-node framework proposed in [11], it relies on the operator partial factorization and on the analysis of a well chosen Schur complement. The selection process of fixing-nodes has been significantly improved to tackle ill conditioned problems. It makes use of graph centrality measures and consider weighted graphs to automatically pick good fixing nodes candidates for heterogeneous problems. Eigen vector, Katz and Page Rank centralities are evaluated and compared with existing approaches. An extension to deal with symmetric indefinite systems arising from mixed finite elements is also presented.

The approach has been assessed on three academic but ill conditioned examples. A comparison with the MUMPS direct solver has been provided showing the good performance of the graph-based strategies. An industrial application is presented, the numerical homogenization of solid propellant. The efficiency of the specific treatment of symmetric indefinite systems has been shown on this application.

Rather specific and often hidden under the hood, this robust process to compute nullspace and generalized inverse of floating subdomains is one of the key component to solve ill-conditioned problems with AMPFETI. It was used in all industrial applications shown in our previous published work, woven composite [4], non associated plasticity [3] and high fidelity multiperforated aircraft combustion chamber involving thermomechanical loading and complex elastoplastic material [5].

We believe that one perspective of this work is to adapt it, to propose a simple, cheap, but efficient method to improve the selection of the FETI-DP corner nodes. Indeed, all subdomains could build a weighted graph associated with the sub-mesh made of few layers of elements touching the interface. The two step process detailed in Section 4, could be used to pick corner-nodes associated with stiff regions of the interface.

# Acknowledgments

The author would like to thanks P. Gosselet and A. Parret-Fréaud for fruitful discussion about the proposed work.

## Financial disclosure

None reported.

## Conflict of interest

The authors declare no potential conflict of interests.

## REFERENCES

[1] P. R. Amestoy I. S. Duff J. Koster and J.-Y. L'Excellent (2001) A Fully Asynchronous Multifrontal Solver Using Distributed Dynamic Scheduling SIAM Journal on Matrix Analysis and Applications **23** no. 1 15–41

[2] Robin Bouclier and Jean-Charles Passieux (2017) A domain coupling method for finite element digital image correlation with mechanical regularization: Application to multiscale measurements and parallel computing International Journal for Numerical Methods in Engineering **111** no. 2 123–143 available at https://onlinelibrary.wiley.com/doi/pdf/10.1002/nme.5456

[3] Christophe Bovet Pierre Gosselet and Nicole Spillane (2017) Multipreconditioning for nonsymmetric problems: The case of orthomin and biCG. Comptes Rendus Mathematique **355** no. 3 354–358

[4] Christophe Bovet Augustin Parret-Fréaud Nicole Spillane and Pierre Gosselet (2017) Adaptive multipreconditioned FETI: Scalability results and robustness assessment Computers & Structures 1–20

[5] Christophe Bovet Augustin Parret-Fréaud and Pierre Gosselet (February 2021) Two-level adaptation for Adaptive Multipreconditioned FETI. Advances in Engineering Software **152** 102952 (en)

[6] D. Brands A. Klawonn O. Rheinbach and J. Schröder (2008October) Modelling and Convergence in Aterial Wall Simulations Using a Parallel FETI Solution Strategy Comput. Meth. Appl. Mech. Engrg. **11** no. 5 569–583

[7] F. Brezzi and Michel Fortin (1991) *Mixed and hybrid finite element methods* Springer series in computational mathematics Springer-Verlag New York

[8] Robert Bridson and Chen Greif (2006) A multipreconditioned conjugate gradient algorithm SIAM J. Matrix Anal. Appl. **27** no. 4 1056–1068 (electronic) MR2205612 (2006i:65044)

[9] William L. Briggs Van Emden Henson and S. F. McCormick (2000) *A multigrid tutorial* 2nd ed Society for Industrial and Applied Mathematics Philadelphia, PA.

[10] Sergey Brin and Lawrence Page (April 1998) The anatomy of a large-scale hypertextual Web search engine Computer Networks and ISDN Systems **30** no. 1-7 107–117 (en)

[11] T. Brzobohatý Z. Dostál T. Kozubek P. Kovář and A. Markopoulos (November 2011) Cholesky decomposition with fixing nodes to stable computation of a generalized inverse of the stiffness matrix of a floating structure International Journal for Numerical Methods in Engineering **88** no. 5 493–509 (en)

[12] Zdeněk Dostál Tomáš Kozubek Alexandros Markopoulos and Martin Menšík (2011) Cholesky decomposition of a positive semidefinite matrix with known kernel Applied Mathematics and Computation **217** no. 13 6067–6077

[13] Zdeněk Dostál David Horák and Radek Kučera (2006) Total feti—an easier implementable variant of the feti method for numerical solution of elliptic pde Communications in Numerical Methods in Engineering **22** no. 12 1155–1162 (en)

[14] Zdeněk Dostál Oldřich Vlach and Tomáš Brzobohatý (April 2019) Scalable TFETI based algorithm with adaptive augmentation for contact problems with variationally consistent discretization of contact conditions Finite Elements in Analysis and Design **156** 34–43 (en) ZSCC: 0000001

[15] Charbel Farhat and Michel Géradin (1998) On the general solution by a direct method of a large-scale singular system of linear equations: application to the analysis of floating structures International Journal for Numerical Methods in Engineering **41** no. 4 675–696 (en)

[16] Charbel Farhat and Francois-Xavier Roux (1991) A method of finite element tearing and interconnecting and its parallel solution algorithm International Journal for Numerical Methods in Engineering **32** no. 6 1205

[17] C. A. Felippa and K. C. Park (March 2002) The construction of free–free flexibility matrices for multilevel structural analysis Computer Methods in Applied Mechanics and Engineering **191** no. 19 2139–2168 (en)

[18] Gene H. Golub and Charles F. Van Loan (2012) *Matrix Computations* JHU Press (en)

[19] Pierre Gosselet Daniel Rixen François-Xavier Roux and Nicole Spillane (2015) Simultaneous FETI and block FETI: Robust domain decomposition with multiple search directions International Journal for Numerical Methods in Engineering **104** no. 10 905–927 nme.4946

[20] T. Hirschler R. Bouclier D. Dureisseix A. Duval T. Elguedj and J. Morlier (2019) A dual domain decomposition algorithm for the analysis of non-conforming isogeometric kirchhoff–love shells Computer Methods in Applied Mechanics and Engineering **357** 112578

[21] Pavla Hruskova (2014) Analysis of fixing nodes used in generalized inverse computation Advances in Electrical and Electronic Engineering **12** no. 2 123–130

[22] Pavla Kabelíková (2010) Graph centers used for stabilization of matrix factorizations Discussiones Mathematicae Graph Theory **30** no. 2 249–259

[23] Pavla Kabelíková (2012) Implementation of Non-Overlapping Domain Decomposition Techniques for FETI Methods

[24] Leo Katz (March 1953) A new status index derived from sociometric analysis Psychometrika **18** no. 1 39–43 (en)

[25] Axel Klawonn and Oliver Rheinbach (2007) Robust FETI-DP methods for heterogeneous three dimensional elasticity problems Computer Methods in Applied Mechanics and EngineerinComputer Methods in Applied Mechanics and Engineering **196** no. 8 1400–1414

[26] Axel Klawonn Oliver Rheinbach and Olof B. Widlund (2008) An analysis of a FETI–DP algorithm on irregular subdomains in the plane SIAM J. Numer. Anal. **46** no. 5 2484–2504

[27] Stefan K. Kleiss Clemens Pechstein Bert Jüttler and Satyendra Tomar (2012) Ieti – isogeometric tearing and interconnecting Computer Methods in Applied Mechanics and Engineering **247-248** 201–215

[28] T. Kozubek V. Vondrák M. Menšık D. Horák Z. Dostál V. Hapla P. Kabelıková and M. Čermák (June 2013) Total FETI domain decomposition method and its massively parallel implementation Advances in Engineering Software **60–61** 14–22

[29] R. Kučera T. Kozubek and A. Markopoulos (2013) On large-scale generalized inverses in solving two-by-two block linear systems Linear Algebra and its Applications **438** no. 7 3011–3029

[30] Michael C. Leistner Pierre Gosselet and Daniel J. Rixen (2018) Recycling of Solution Spaces in Multi-Preconditioned FETI Methods Applied to Structural Dynamics International Journal for Numerical Methods in Engineering

[31] E. Lorentz (December 2008) A mixed interface finite element for cohesive zone models Computer Methods in Applied Mechanics and Engineering **198** no. 2 302–317

[32] Jan Mandel and Bedřich Sousedík (2007) Adaptive selection of face coarse degrees of freedom in the BDDC and the FETI-DP iterative substructuring methods Comput. Methods Appl. Mech. Engrg. **196** no. 8 1389–1399

[33] A. Markopoulos L. Říha T. Brzobohatý P. Jirůtková R. Kučera O. Meca and T. Kozubek (2017) Treatment of singular matrices in the hybrid total feti method Domain decomposition methods in science and engineering xxiii Springer International Publishing 237–244

[34] Michal Merta Lubomir Riha Ondrej Meca Alexandros Markopoulos Tomas Brzobohaty Tomas Kozubek and Vit Vondrak (2017) Intel xeon phi acceleration of hybrid total feti solver Advances in Engineering Software **112** 124 –135

[35] Roberto Molina and François-Xavier Roux (2019) New implementations for the Simultaneous-FETI method International Journal for Numerical Methods in Engineering **118** no. 9 519–535

[36] M. E. J. Newman (2018) *Networks* Second edition Oxford University Press Oxford, United Kingdom ; New York, NY, United States of America

[37] M. Papadrakakis and Y. Fragakis (2001) An integrated geometric–algebraic method for solving semi-definite problems in structural mechanics Computer Methods in Applied Mechanics and Engineering **190** no. 49–50 6513–6532

[38] Lubomír Říha Tomás Brzobohatý Alexandros Markopoulos Ondrej Meca and Tomás Kozubek (2016) Massively parallel hybrid total feti (htfeti) solver Pasc 16

[39] N. Spillane (2014) *Robust domain decomposition methods for symmetric positive definite problems* Ph.D. Thesis

[40] Nicole Spillane (2016) An Adaptive Multipreconditioned Conjugate Gradient Algorithm SIAM J. Sci. Comput. **38** no. 3 A1896–A1918

[41] Nicole Spillane and Daniel J. Rixen (2013) Automatic spectral coarse spaces for robust FETI and BDD algorithms International Journal for Numerical Methods in Engineering **95** no. 11 953–990

[42] A. Suzuki and F.-X. Roux (2014) A dissection solver with kernel detection for symmetric finite element matrices on shared memory computers International Journal for Numerical Methods in Engineering **100** no. 2 136–164

[43] Jari Toivanen Philip Avery and Charbel Farhat (2018) A multilevel FETI-DP method and its performance for problems with billions of degrees of freedom International Journal for Numerical Methods in Engineering **116** no. 10-11 661–682 (en)

[44] Fuzhen Zhang (2005) *The schur complement and its applications* Numerical methods and algorithms Springer New York

[45] O. C. Zienkiewicz Robert L. Taylor and David Fox (2014) *The finite element method for solid and structural mechanics* 7th ed Elsevier/Butterworth-Heinemann Amsterdam ; Boston

**How cite this article:** C. Bovet (2021), Title, *Int. J. Numer. Meth. Engng.*, *2021;00:1–6.*